Lattice gauge theory and dynamical quantum phase transitions using noisy intermediate-scale quantum devices

Simon Panyella Pedersen [1,*] and Nikolaj Thomas Zinner [1,2,†]

[1]*Department of Physics and Astronomy, Aarhus University, DK-8000 Aarhus C, Denmark*
[2]*Aarhus Institute of Advanced Studies, Aarhus University, DK-8000 Aarhus C, Denmark*

Lattice gauge theories are a fascinating and rich class of theories relating to the most fundamental models of particle physics, and as experimental control on the quantum level increases there is a growing interest in nonequilibrium effects such as dynamical quantum phase transitions. To demonstrate how these physical theories can be accessed in near-term quantum devices, we study the dynamics of a $(1 + 1)$D U(1) quantum link model following quenches of its mass term. We find that the system undergoes dynamical quantum phase transitions for all system sizes considered, even the smallest where the dynamics can be solved analytically. We devise a gauge-invariant string order parameter whose zeros correlates with the structure of the Loschmidt amplitude, making the order parameter useful for experimental study in near-term devices. The zeros of the Loschmidt amplitude as well as the zeros of our order parameter are revealed by vortices in their phases, which can be counted by a topologically invariant winding number. With noisy intermediate-scale quantum devices in mind, we propose a class of superconducting circuits for the general implementation of U(1) quantum link models. The principles of these circuits can be generalized to implement other, more complicated gauge symmetries. Furthermore, the circuit can be modularly scaled to any lattice configuration. Simulating the circuit dynamics with realistic circuit parameters, we find that it implements the target dynamics with a steady average fidelity of 99.5% or higher. Finally, we consider readout of the circuit using a method that yields information about all the degrees of freedom with resonators coupled dispersively to only a subset of them. This constitutes a direct and relatively straightforward protocol to access both Loschmidt amplitudes and the order parameter.

I. INTRODUCTION

There is an increasing study of nonequilibrium quantum dynamics as improving experimental quantum control makes it accessible [1]. Quantum simulators have been realized with cold atoms in optical lattices, ions, and superconducting quantum circuits (SQCs), among others, and have already been used to study exciting dynamical phenomena like time crystals [2,3], many-body localization [4,5], prethermalization and thermalization [6–8], and particle-antiparticle creation and annihilation [9]. In particular, an interest in dynamical quantum phase transitions (DQPTs) is emerging [10–22]. These occur when the Loschmidt amplitude $\mathcal{G}(t) = \langle \psi(0)|\psi(t)\rangle$, which is the overlap between the initial state and the state at time t, becomes zero or shows nonanalytic behavior. In the context of DQPTs, $\mathcal{G}(t)$ formally takes the place of a partition function. These points of vanishing or nonanalytic behavior happen in the proper time evolution of the system, and herald a transition between dynamical phases. This is to be compared with equilibrium phase transitions which are heralded by nonanalytical behavior occurring as system properties are externally changed [23]. DQPTs have been studied experimentally [24–27] and offer a broad spectrum of fascinating

physics, like a connection to topology [28–31], allowing for the definition of dynamical topological order parameters [27,32,33], vortex dynamics [34], scaling and universality [11] and both showing a connection to underlying equilibrium phase transitions [10,29,35] as well as being completely independent of them [36–39] (the latter showing their truly nonequilibrium nature). An interesting type of system for the study of dynamics is gauge theories, specifically lattice gauge theories (LGTs) [40–42]. Gauge theories are at the basis of our understanding of particle physics and are notoriously difficult to handle both analytically and numerically. They are thus ideally suited for analog simulation [43–50]. Recently, a method for extracting defining information about a quantum field theory from experimental data was proposed [51,52]. Furthermore, a direct observation of U(1) gauge invariance and an equilibrium phase transition in a 71-site ultracold atom system was reported in Ref. [53]. DQPTs in gauge theories, on the other hand, have been studied numerically [17,31], as well as analytically in the noninteracting limit in Ref. [31], but have yet to be observed experimentally to the best of our knowledge.

In this work, we show how to obtain LGTs, in the form of quantum link models (QLM) [17,43,54–57], in SQCs in a fully consistent way, showing that we get the desired Hamiltonians with very high fidelity. We use the example of U(1) to demonstrate this, and we show that exploring the field of DQPTs is possible with NISQ-era devices [58]. We study

*spp@phys.au.dk
†zinner@phys.au.dk

a particular U(1) symmetric system, the massive Schwinger model [9,31,59–61], which exhibits DQPTs after a quench for all system sizes considered. A recent study by Zache *et al.* has considered DQPTs in continuum and LGT models. In Ref. [31], DQPTs were found through the study of vorticity in an appropriate order parameter, implying that the transitions have a topological nature. Here, we consider a QLM over a larger range of parameters and write down a gauge-invariant string order parameter that is accessible even in small systems of relevance in near-term quantum devices. We show how the zeros of both this order parameter as well as those of the Loschmidt amplitude can be found by looking for vortices in their respective phases. The zeros of the order parameter correlate for all system sizes with the low points of the Loschmidt amplitude

In the second part of this paper, we propose a superconducting quantum circuit, which through use of the eigenmodes of the capacitive network [62–66] implements three spin-1/2's interacting via Z-type couplings (i.e., couplings consisting solely of products of Pauli-Z matrices) and a direct three-body XXX coupling. Through appropriate tuning, the XXX coupling yields the desired U(1) invariant interaction necessary for the analog simulation of a U(1) QLM. The Z-type couplings essentially just shift the energy levels of the system and do not disturb the desired feature of the circuit but merely make more complicated numerical tuning necessary. We find that with appropriately tuned parameters the circuit implements the desired dynamics with an average fidelity of about 99.5% or higher, with most of the loss caused by leakage to higher levels, which could be further suppressed at the cost of slower dynamics. The circuit can be scaled in a modular way to construct any desired spin lattice configuration. Furthermore, we provide a readout scheme for how to observe this in concrete setups, inspired by that of Refs. [64,65]. This makes it possible now to use NISQ devices to do precision studies of LGTs and DQPTs.

In Sec. II, we discuss the QLM, the quench of the mass, and our order parameter. In Sec. III, we show our method for finding the zeros of the Loschmidt amplitude and our order parameter by looking at vortices in their phases. Section IV contains our numerical results concerning these quantities, showing how even at the smallest system size considered we see DQPTs and vortex dynamics. In Sec. V, we introduce and analyze the circuit used to implement the direct XXX coupling. We then discuss tuning of the circuit parameters in Sec. VI, showing an example in the Supplemental Material [67] of viable circuit parameters which yield good spin model parameters for the simulation of the quench dynamics discussed in the first part of the paper. In Sec. VII, we then go through our proposal for readout of the circuit with intent to perform quantum state tomography. Finally, in Sec. VIII, we summarize and conclude the paper.

II. SYSTEM AND PROCEDURE

A. Hamiltonian

In this work, we study an example of an interacting LGT, specifically the $(1 + 1)$D U(1) gauge theory, on a periodic lattice. We represent the fermionic field with spinless, staggered mass fermions on the sites of the lattice, and transform these via the Jordan-Wigner transformation [57,68–70] into spin-1/2's. We will be working in the quantum link model framework, where gauge fields, living on the links of the lattice, are represented by spin-1/2's. Thus, the entire model is represented by a spin-1/2 system. The Hamiltonian for this system is

$$H = \sum_{n=0}^{N-1} \left[-(-1)^n \frac{m}{2} \sigma_n^z + \frac{J}{2} (\sigma_n^+ S_{n,n+1}^+ \sigma_{n+1}^- + \text{H.c.}) \right], \quad (1)$$

where N is the number of matter sites, which must be even to conserve the symmetry between particles and antiparticles, m is the staggered mass of the fermions, and J is the matter-gauge coupling strength. The $J/2$ coefficient is usually written as $1/2a$, where a is the lattice spacing. However, since we are not interested in the continuum limit $a \to 0$, we prefer to think of the coefficient as a coupling strength, $J = 1/a$. σ_n^α with $\alpha = z, +, -$ are Pauli-Z, step-up, and step-down matrices pertaining to the matter field spin at site n. Likewise, $S_{n,n+1}^\alpha$ for $\alpha = z, +, -$ are spin operators for the gauge field spin on the link connecting site n and site $n + 1$. The electric field energy term $E_{n,n+1}^2 \sim (S_{n,n+1}^z)^2$ has been neglected because it is constant, when the gauge field is represented by spin-1/2's. The sign in front of $(-1)^n \frac{m}{2} \sigma_n^z$ is to make $(1, 0)^T$ and $(0, 1)^T$ the ground and excited states respectively for even n. Our $\sigma^\pm$ are correspondingly defined. We will consider quenches of the sign of the mass $m \to -m$; i.e., we will initialize in the ground state of the above Hamiltonian, and then perform time evolution with the Hamiltonian where the sign of the mass has been switched. This corresponds to a maximal quench of the vacuum angle. The vacuum angle is a parameter that may be included in quantum chromodynamics as well as the Schwinger model, relating to the nontrivial structure of their vacua [71,72] and quantifying a charge-parity symmetry violating term. For more information, see Refs. [60,71–78]. However, we will not consider the vacuum angle itself but rather focus on the quench and the subsequent DQPTs. Explicitly, we will be initializing the system in the ground state of the prequench Hamiltonian $H_i = H(m, J)$ at time $t = 0$ and then perform unitary time evolution according to the postquench Hamiltonian $H_f = H(-m, J)$. We study the postquench dynamics by looking at the Loschmidt amplitude $\mathcal{G}(t)$ or Loschmidt echo $\mathcal{L}(t) = |\mathcal{G}(t)|^2$, as well as an order parameter introduced below.

B. Symmetries

The system has several symmetries which are conserved across the quench. We will therefore be simplifying numerical simulation by only working in the symmetry sector of the Hilbert space, to which the initial state belongs. The system, of course, has a local U(1) symmetry, generated by

$$G_n = S_{n-1,n}^z - S_{n,n+1}^z + \sigma_n^z - (-1)^n.$$

We will be working in the gauge sector of no background charges, i.e., the physical states satisfy $G_n|\text{phys}\rangle = 0$ for all n. Furthermore, the system has parity and charge conjugation

symmetries, P and C, implemented as

$$\sigma_n^z \xrightarrow{P} \sigma_{-n}^z, \qquad\qquad \sigma_n^{\pm} \xrightarrow{P} \sigma_{-n}^{\pm},$$

$$S_{n,n+1}^z \xrightarrow{P} -S_{-n-1,-n}^z, \qquad S_{n,n+1}^{\pm} \xrightarrow{P} S_{-n-1,-n}^{\mp},$$

$$\sigma_n^z \xrightarrow{C} -\sigma_{n+1}^z, \qquad\qquad \sigma_n^{\pm} \xrightarrow{C} \sigma_{n+1}^{\mp},$$

$$S_{n,n+1}^z \xrightarrow{C} -S_{n+1,n+2}^z, \qquad S_{n,n+1}^{\pm} \xrightarrow{C} S_{n+1,n+2}^{\mp},$$

where the subscript index is calculated as modulus N. These symmetries satisfy $P^2 = C^N = 1$. The fact that C is cyclic is a consequence of the periodic boundaries of our system. The symmetries make it possible to solve the dynamics analytically for small system sizes, $N = 2, 4$. That is, the Hilbert space can be divided into symmetry sectors with different eigenvalues for each of the symmetries, with so few states in each of them that they can each be analytically diagonalized. The diagonalization boils down to solving a characteristic polynomial equation as is standard. As is well known by Galois theory, this implies that for polynomial degree of 4 or smaller, the solution can be given in rational form. For $N = 6$, the sector containing the ground state we initialize in already has five states. For the analytical solution of the $N = 2, 4$ systems, see the Supplemental Material [67]. For $N = 2$, it is even possible to analytically determine the zeros of $\mathcal{G}(t)$ and thus the times of the DQPTs.

Because of these symmetries, the periodicity of the system, and the state we initialize in, it can furthermore be shown that (see the Supplemental Material [67])

$$\langle \sigma_n^z \rangle = (-1)^n \langle \sigma_0^z \rangle, \quad \langle S_{n,n+1}^z \rangle = (-1)^n \frac{\langle \sigma_0^z \rangle - 1}{2}. \quad (2)$$

This is essentially a consequence of the fact that we have periodic boundaries, and so the system is symmetric under stepwise rotations; i.e., all particle sites must have the same dynamics, and likewise for antiparticle sites. Coupled together with the fact that we are working in the sector of equally many particles and antiparticles (zero total charge), we get the above relation between the $\langle \sigma_n^z \rangle$. The relation for the gauge link spins is a consequence of fact that the dynamics of the gauge fields are completely determined by the matter fields in a spin-1/2 QLM. Furthermore, $\langle \sigma_n^\beta \rangle = \langle S_{n,n+1}^\beta \rangle = 0$ for $\beta = x, y$ and all n, which follows simply from the fact that σ_n^β, $S_{n,n+1}^\beta$ are gauge *variant*, and so their expectation value within a certain gauge sector is zero. This means that a single measurement of σ^z for any spin in the system reveals the equivalent quantity for all spins in the system, and only σ^z yields a nonzero measurement. This will be a decisive observation for the readout scheme in an experimental realization.

C. Order parameter

The order parameter we use to study the postquench dynamics is $g(k, t) = \langle \psi(0) | \mathfrak{g}(k) | \psi(t) \rangle$, where

$$\mathfrak{g}(k) = \sum_{m=0,1} \sum_{n=0}^{N-1} e^{-ik d_m(n)} \sigma_m^- \prod_{i=m}^{n-1} S_{i,i+1}^{\alpha_m(n)} \sigma_n^+.$$

This is a sum over two representative sites $m = 0, 1$ (a particle site and an antiparticle site respectively) and over all sites of
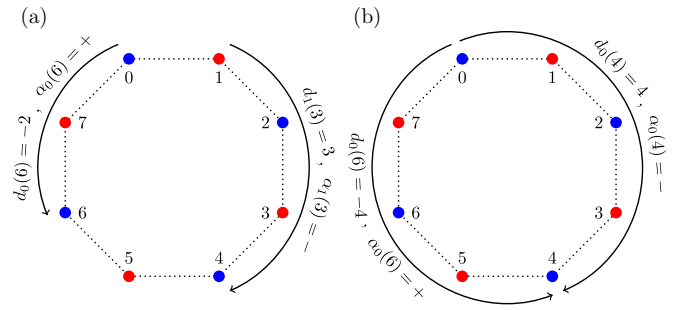

FIG. 1. Some examples of the paths taken by the string operators which are summed over in the order parameter for a system size of $N = 8$ matter sites. (a) Two examples, on originating from particle site 0 and the other from the antiparticle site 1, showing the sign conventions for clockwise and counterclockwise paths. (b) An example of the case where $m - n = N/2$, where the equidistant clockwise and counterclockwise paths are both taken into account.

the lattice $n = 0, \ldots, N - 1$. The summand is a Fourier coefficient times a string operator, consisting of two matter site operators, one at the representative site m and the other at n, connected by the gauge link operators between the two sites, making the total operator gauge invariant. Here the products of link operators are over the *shortest* path between site m and site n, i.e., either counterclockwise or clockwise along the circular lattice; see Fig. 1. Likewise $d_m(n)$ is the distance from site m to n along the shortest path, with $d_m(n)$ being positive for clockwise paths and negative for counterclockwise paths. Similarly, $\alpha_m(n) = -$ for clockwise paths and $\alpha_m(n) = +$ for counterclockwise paths, ensuring the gauge invariance of the summands. For sites on the exact opposite side of the circular lattice, i.e., $m - n = N/2$, the two paths around the lattice are equidistant and so both are included; see Fig. 1(b). Thus, the operator $\mathfrak{g}(k)$ is essentially the Fourier transform of the gauge-invariant string operators connecting the sites 0 and 1 with all sites of the lattice. The order parameter $g(k, t)$ is then the Fourier transform of the amplitudes of a matter excitation moving from either site 0 or 1 to site n, via the shortest path, in the time between initialization and t. The reason we have both a term for site 0 and one for site 1 is to make the operator symmetric with respect to particles and antiparticles. The Fourier parameter k takes its value in the Brillouin zone $[-\pi/a, \pi/a]$, though the periodic boundaries of the system makes the order parameter symmetric around $k = 0$. We therefore only consider $k \in [0, \pi/a]$. We define the phase ϕ_g of the order parameter via $g = |g| e^{i\phi_g}$. As we will see, this order parameter has zeros along the troughs of the Loschmidt echo, $\mathcal{L}(t)$, for all system sizes. These zeros are accompanied by vortices in ϕ_g, which can be counted by a winding number. The vortices show an interesting dynamics of creation and annihilation as the coupling constant is varied. Hence, even in the smallest interesting system, this order parameter reveals the structure of $\mathcal{L}(t)$, which repeats itself as the system size is increased and exhibits nontrivial vortex dynamics. The order parameter that we employ here is related to the gauge-invariant time-ordered Green's function computed in the context of lattice gauge theory in Ref. [31], which was shown to reduce to the Loschmidt amplitude in the noninteracting case, and be correlated with the Loschmidt
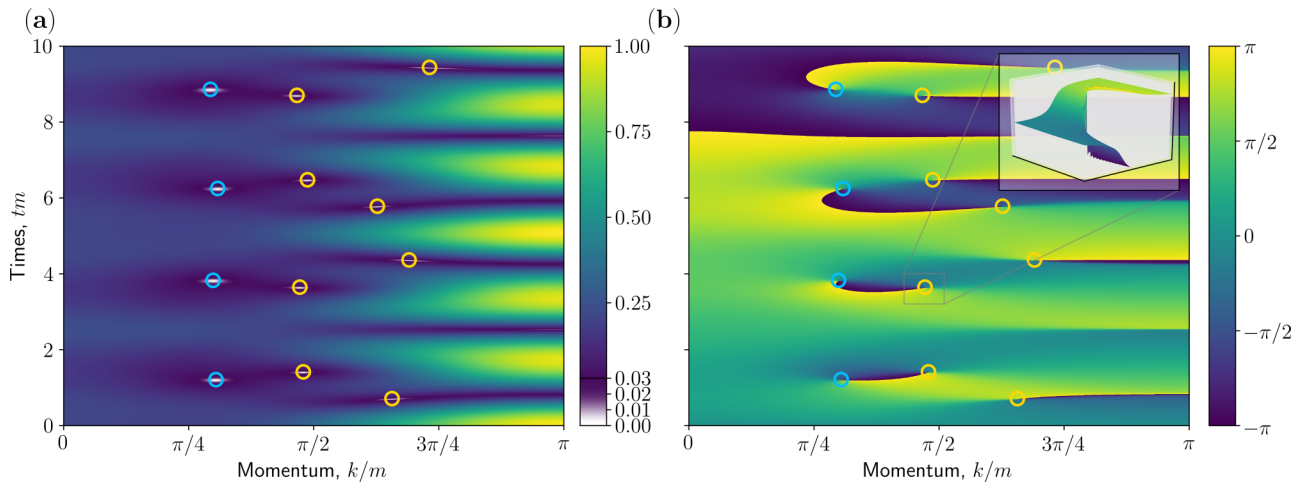
FIG. 2. (a) The modulus $|g|$ and (b) the phase ϕ_g of the order parameter g for $N = 4$ and $J/m = 1.95$. The vortices of the phase, corresponding to the zeros of g, as found by the method described in the text, have been marked with circles colored blue for right-winding vortices and yellow for left-winding. In the inset, a 3D enlargement of a vortex can be seen, rotated to put the tear clearly into view.

amplitude in the interacting case. Our work demonstrates how to transfer this to QLM models.

III. COUNTING VORTICES

We study the dynamics of the Loschmidt amplitude and the order parameter introduced above over a range of the coupling strength J (keeping m fixed) and a range of the system size N. We are in particular interested in the zeros of these quantities. Considering $\mathcal{G}(t)$ as a complex function in the (J, t) plane and g a complex function in the (k, t) plane (with J fixed), we can find their zeros in a similar fashion, namely by looking at their phase. This method for numerically finding the vortices is an adaptation of the work in Ref. [79], developed for computing Chern numbers in momentum space. When a complex function, say $f = re^{i\varphi}$, becomes zero at some critical point, its phase φ is undefined at that point. For a complex function of two variables, $f = f(x, y)$, this results in a vortex in φ surrounding the critical point; see the inset of Fig. 2(b) showing a vortex in the phase of $g(k, t)$. The intuition of this is that while φ is undefined at the critical point it is otherwise smooth, up to discontinuities of 2π. If there were no discontinuity around the critical point there would obviously be a meaningful, smooth extension of φ at the undefined point, which contradicts the fact that φ is undefinable. The phase must thus have a line of 2π discontinuity extending from the critical point. Starting at this discontinuity and going around the critical point, φ must then attain all possible values between $-\pi$ and π in a smooth way, as there would otherwise again be a meaningful, smooth extension of φ. Such vortices can be counted by a winding number

$$\nu = \frac{1}{2\pi} \oint_{\mathcal{C}} d\boldsymbol{l} \cdot \nabla \varphi,$$

where $\mathcal{C}$ is a closed curve. This number may then be considered a dynamical topological order parameter [27,32], as it is a parameter changing its value with time, taking on discrete values which only depend on the topology of φ, i.e., its vortices, and whether $\mathcal{C}$ encloses these vortices. Closing such a

curve tightly around a vortex, the winding number essentially detects that a line of 2π discontinuity enters the area enclosed by the curve without exiting again. Together with the image of the vortices always being tailed by these lines, which we will refer to as tears (as in torn fabric), we see that to find the vortices we must simply be able to identify the tears and their ends. The tears can only end either at the edge of the considered parameter space or at a vortex. Hence, one only needs sufficient resolution (in a simulated or experimental data) to distinguish discontinuous jumps of 2π from the jumps between the data points on a coarse grid in order to find the zeros of the function f. This makes it possible to find and study zeros and vortices with a minimal numerical computational effort, and we have used an algorithm based on this idea to do so in our system. Furthermore, one can be certain that these will be true zeros of the function and not points where the complex function merely has a very small modulus. This is otherwise in principle quite hard to do, as unavoidable numerical imprecision would usually make it necessary to set an arbitrary limit on when the modulus is small enough to indicate that the function has actually become zero.

IV. SIMULATION OF DYNAMICS

A. Dynamics of g

In Fig. 2, we show an example of the modulus and phase of g for a system size of $N = 4$ and a coupling strength of $J/m = 1.95$. The zeros of g, as found by the approach described in the previous section, clearly do correspond uniquely to $|g|$ becoming very small, confirming the method. Furthermore, looking at the plot of ϕ_g, the strength of this approach becomes clear. It is easy to see that the tears in ϕ_g end in vortices or at the edge of the Brillouin zone, and it is therefore easy to find the zeros of the order parameter. The inset shows a 3D enlargement of a vortex. This shows how the 2π discontinuity ends at a point where the surface plot of ϕ_g is a vertical line, i.e., where ϕ_g is undefined, and surrounding this point the surface goes smoothly from $-\pi$ to π in a helix structure.
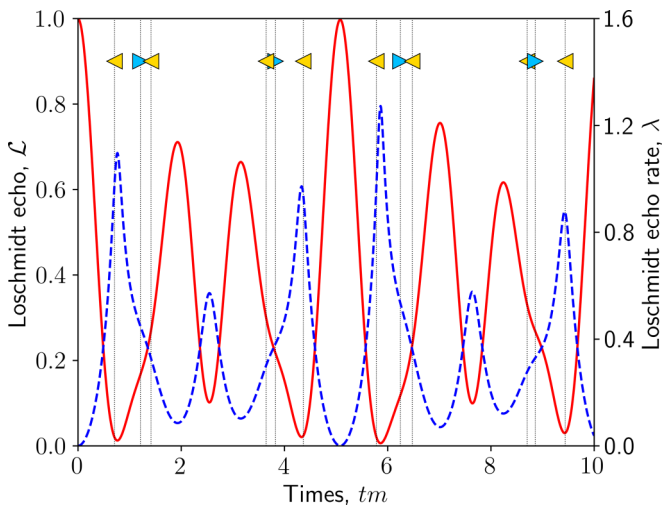
FIG. 3. The Loschmidt echo $\mathcal{L}(t)$ (solid red line) and its rate function $\lambda(t)$ (dashed blue line), following the mass quench, $m \to -m$ with the same system parameters as in Fig. 2. The vertical dotted lines indicate the times at which vortices occur in g, and the triangular arrow heads indicate the orientation of the vortices, with arrow heads pointing right, indicating right-winding vortices, and arrow heads pointing left for left-winding vortices. There is a clear correlation between the deepest minima of $\mathcal{L}(t)$ [the sharpest peaks of $\lambda(t)$] and the appearance of vortices, except when the vortices come in pairs of opposite orientation. For slightly larger J/m, vortices appear at times corresponding to the two minima of $\mathcal{L}(t)$ [two peaks of $\lambda(t)$] at $t \approx 2.5, 7.5$.

Figure 3 shows the Loschmidt echo $\mathcal{L}(t)$ for the parameters in Fig. 2. The time of the vortices in ϕ_g are marked with vertical dashed lines and triangular, colored arrow heads, indicating the orientation of the vortices. While we find that the vortices in ϕ_g generally appear at values of (J, t) where $\mathcal{L}(t)$ is small, we find that vortices of opposite winding which are close in the (k, t) plane can be found at larger values of $\mathcal{L}(t)$. Intuitively, one might think of the vortices as charges, and when two charges of opposite sign are near each other,

they screen each other off. There are some additional dips at approximately $tm = 2.5, 7.5$ not accompanied by vortices. However, for slightly larger J/m, vortices will appear at these dips. This temporary discrepancy is caused by the fact that $\mathcal{L}(t)$ varies smoothly as a function of J/m, while the appearance and disappearance of vortices is sudden.

Looking at ϕ_g for different J/m, these vortices "move" in the (k, t) plane, being created or annihilated in pairs of opposite orientation, or appearing and disappearing at the edges of the Brillouin zone. This is how ϕ_g changes its number of vortices in integer steps. In Fig. 4 are 10 plots of ϕ_g for different consecutive values of J/m. At first we see three tears stretching across the entire plot, but as J/m is increased these tears detach from the right and left sides of the Brillouin zone, via the creation of respectively left-winding and right-winding vortices at their ends. These vortices remain connected by the tear until they annihilate either with other, other vortices, or disappear again at the edges. At $J/m = 1.4$, a pair of vortices is created at $tm \simeq 7$ and $k/m \simeq 3\pi/4$. Thus, we see how vortices appear and disappear at the edges or are created in pairs, how they annihilate with each other, and how they are always trailed by a tear whose ends must be at the edges or at a vortex. Such vortex dynamics is known from other systems, for example, Berezinskii-Kosterlitz-Thouless transitions, both in equilibrium and nonequilibrium [80–83].

B. Dynamics of $\mathcal{L}$

In Fig. 5, $\mathcal{L}(t)$ can be seen for the considered range of J/m and t, for system sizes $N = 4, 8, 16$. The zeros of $\mathcal{L}(t)$ are marked with circles using the same color code as previously. Most of them are left winding with a few right winding at late times in the middle and lower frames of Fig. 5. It is unclear whether the orientation of the vortices in the phase of $\mathcal{G}(t)$ has any physical significance or whether it is simply a mathematical detail. In the phase of the order parameter ϕ_g, we saw dynamics of the vortices including annihilation of oppositely winding vortices as function of J/m, but we cannot speak of something similar in the phase of $\mathcal{G}(t)$. The zeros of $\mathcal{L}(t)$ are found by applying the method described in the previous
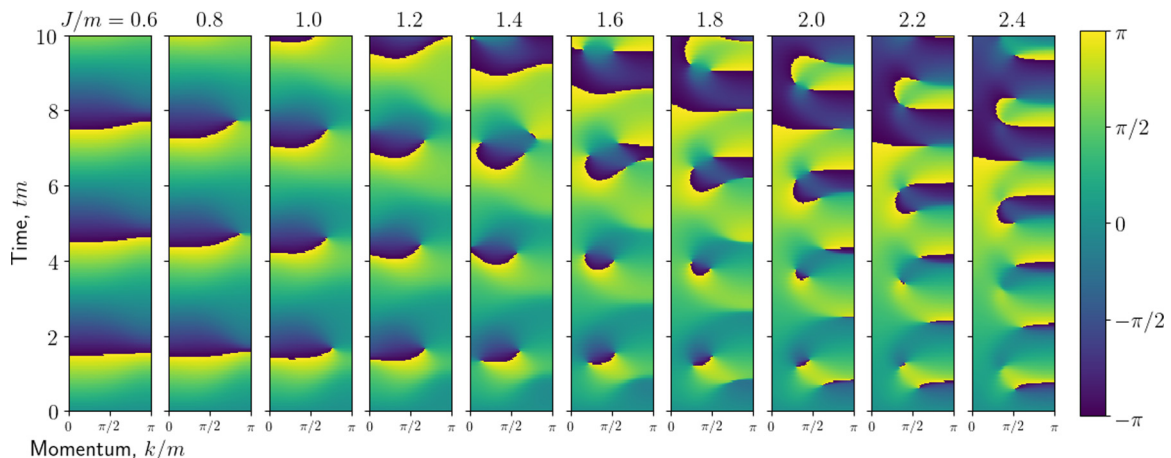

FIG. 4. Ten plots of ϕ_g showing the dynamics of its vortices. Following the three tears extended across the first plot as J/m increases, we see how they detach from the edges of the Brillouin zone via the creation of vortices and how these vortices eventually annihilate with each other, with other vortices, or disappear at the edges. We can also see the creation of a pair of vortices at $J/m = 1.4$, $tm \simeq 7$, $k/m \simeq 3\pi/4$.
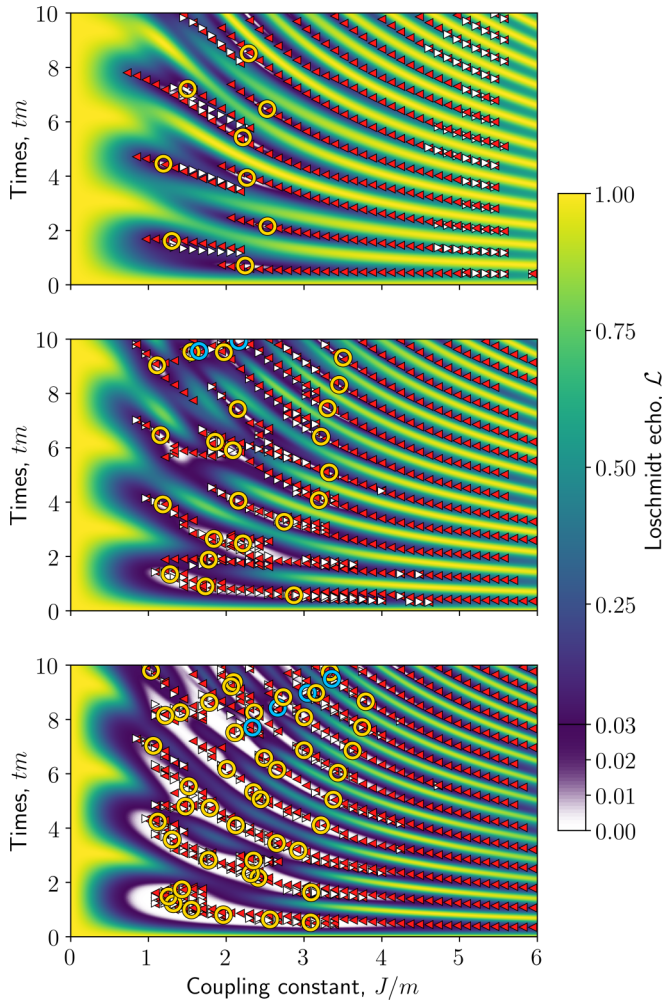
FIG. 5. Contour plots of $\mathcal{L}(t)$ for the considered range of J/m and t, for system sizes $N = 4, 8, 16$ from top to bottom. The zeros, as found by considering vortices in the phase of $\mathcal{G}(t)$, are marked with circles colored blue for right-winding vortices and yellow for left-winding. A representative set of the vortices of the order parameter are plotted with arrow heads. White arrow heads indicate right-winding vortices, and red arrow heads indicate left-winding vortices. Particularly for $N = 4$, it can be clearly seen how vortices of opposite orientation move around the (J, t) plane and annihilate. The structure of $\mathcal{L}(t)$ and its zeros has a clear pattern that is present in all three plots. For $N = 16$ $\mathcal{L}(t)$, is very close to zero in large areas, and its zeros, particularly at early times, trace out a curve following the center of these lobes.
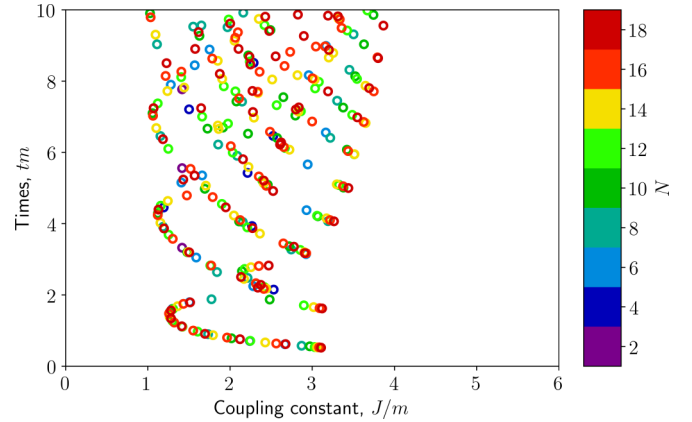

FIG. 6. All vortices of $\mathcal{G}(t)$ for all considered system sizes plotted together as circles, with a color code denoting which N each data point pertains to. Some patterns and curves emerge here, particularly for early times.

section to the phase, $\phi_{\mathcal{G}(t)}$, of $\mathcal{G}(t)$. The zeros of the order parameter are also shown in Fig. 5, indicated with triangles and a different color code for distinguishability. We can see how the zeros of the order parameter lie along the troughs of $\mathcal{L}(t)$, and for $N = 4$ in the upper panel of Fig. 5 it is particularly clear in, for example, the region $1 < J/m < 2$ how vortices in ϕ_g of opposite orientation move and annihilate as function of J/m. There is a clear pattern of $\mathcal{L}(t)$ being small in large lobes that start at around $J/m = 0.5$ and stretch toward higher J/m while $\mathcal{L}(t)$ increases. The zeros of $\mathcal{L}(t)$ occur near the center of these lobes, along lines which are traced out by the zeros of the order parameter. This pattern appears already

at $N = 4$ and repeats itself for larger system sizes, showing see how the small system with $N = 4$ reproduces features of the much larger $N = 16$ system. This means that even a small experimental realization of this system could yield interesting results. We discuss this possibility in greater detail later in the paper. While the even smaller system with $N = 2$ does show zeros both in g and $\mathcal{L}(t)$, the behavior of these is considerably different and simpler than for larger N; see Supplemental Material [67]. We explain this different behavior by the fact that, as mentioned, the system is completely solvable for such a small size and the zeros of $\mathcal{L}(t)$ can found analytically.

For increasing system size $\mathcal{L}(t)$ becomes very small in increasingly larger areas and has more zeros. The large areas of small value can be explained by the scaling of $\mathcal{L}(t) = e^{-N\lambda(t)}$, where $\lambda(t)$ is the rate function of the Loschmidt echo, which converges in the thermodynamic limit of $N \to \infty$. That is, the Loschmidt echo is exponentially suppressed by the system size and thus naturally becomes very small for large systems. The zeros of $\mathcal{L}(t)$ appear to arrange themselves along curves tracing out the center of the lobes where $\mathcal{L}(t)$ is small. In Fig. 6, the zeros of $\mathcal{L}(t)$ are plotted together for all the considered N. Especially for small t there is a clear hook-shaped curve along which the zeros arrange themselves. A similar pattern seems to repeat itself a few times for larger t, defining branches of zeros. While the exact position on the branches of the individual zeros is dependent on N, the branches do become more defined (at least for small t) for increasing N, where the number of zeros also increases. This condensation of discrete vortices is similar to how the zeros of a partition function are known to converge to lines in the thermodynamic limit [10,15,21,29,84]. A plot of $\lambda(t)$ for each N considered is shown in the Supplemental Material [67], including an enlargement where the formation of the line of zeros at early times can be clearly seen. The occurrence and quick converge of these lines beginning already at $N = 4$ shows how the interesting dynamical effects of our system are not just finite-size effects but from early on reflect the dynamics of the thermodynamic limit.

Figure 6 furthermore clearly shows how the zeros of $\mathcal{L}(t)$ occur within an interval of J/m that expands slowly for

increasing tm. For both $J/m \ll 1$ and $J/m \gg 1$, we expect $\mathcal{L}(t)$ to go unity. This is because for $J/m \ll 1$ the mass term dominates and so the prequench ground state is still close to being an eigenstate of the postquench Hamiltonian (the sign of its energy will simply have changed). For $J/m \gg 1$, the interaction term dominates and so the prequench ground state is still the ground state after the quench, as the interaction term does not change in the quench. For these reasons, it makes sense that there is a limited interval of J/m in which the zeros occur. We expect this interval to expand for increasing tm, simply because the weak or suppressed dynamics responsible for the zero will have more time to occur. For the same reasons, we expect the order parameter to not show vortices in these limits, which is consistent with Fig. 5.

C. Possibility of underlying equilibrium transition

One of the most observed cases for what causes a DQPT is quenches across some underlying equilibrium phase transition [21]. However, given that the DQPTs we observe occur at unsystematic values of J/m and are dependent on the system size, it is difficult to see how an equilibrium phase transition should be the cause of the DQPTs. Furthermore, while equilibrium phase transitions are often discovered by looking at average magnetizations and similar quantities, in our periodic system we have found that $\langle \sigma_n^z \rangle = (-1)^n \langle \sigma_0^z \rangle$ and $\langle S_{n,n+1}^z \rangle = (-1)^n (\langle \sigma_0^z \rangle - 1)/2$, meaning that any average of these is identically zero. Indeed, since all expectation values of σ^z for both sites and links are given by $\langle \sigma_0^z \rangle$, and expectation values of σ^x, σ^y for sites and links are zero (since they are gauge variant), the only local variable we could study is indeed $\langle \sigma_0^z \rangle$. Alternatively, it might be possible to devise a gauge-invariant, nonlocal order parameter, similar to $g(k, t)$, which captures an equilibrium phase transition that is the cause of the DQPTs we have found here. We expect such an order parameter to be topological in nature, and thus the equilibrium phase transition to topologically nontrivial. In this context, the Kibble-Zurek mechanism [85,86] might be relevant to consider to relate a possible equilibrium transition to the DQPTs we see [87,88]. Whether an underlying transition is the cause of the observed DQPTs and how such a transition should be revealed are interesting questions for future research in our system.

V. CIRCUIT REALIZATION OF QLM

To realize a QLM, you need discrete sites arranged in a lattice, with links connecting them in some configuration. On the sites live matter field degrees of freedom, which for a fermionic field is equivalent to a discrete two-level system, as discussed above. Likewise, on the links live finite degrees of freedom, spin-S subsystems, representing the gauge field coupling the matter fields. Compared to LGTs, where the gauge fields have an infinite number of degrees of freedom, the advantage of QLMs is thus a vastly reduced Hilbert space as a consequence of the finite number of states available to the gauge field. The QLM are valid and interesting gauge theories in themselves but can also be seen as an approximation of LGTs, as an LGT is recovered by letting $S \to \infty$.

We now go on to discuss a possible experimental implementation of U(1) symmetric spin-1/2 systems using SQCs.

We present a circuit which implements two matter site spins and a gauge link spin interacting via a direct three-body XXX coupling, which through appropriate tuning yields the desired U(1) interaction in the rotating wave approximation (RWA). The circuit scales naturally in a modular fashion and could be used to create 1D chains, 2D lattices, or any other configuration of matter sites interacting through gauge links. Hence, the circuit could be used to experimentally implement dynamics in 1D or 2D models to study, for example, vacuum quenches similar to what we looked at above or strong CP breaking in gauge models. Figure 7(c) shows a diagrammatic implementation of a plaquette of four sites, hinting at how a 2D configuration would have to be made. Early work was done to indicate that circuits could be used for simulating LGTs [70,89–97], but this work did not consider concrete cases in detail nor any checks on whether the circuits actually realize the right dynamics with high fidelity. In the next section, we directly compare the time evolution operator implemented by our circuit with the desired time evolution operator of the U(1) spin-1/2 QLM presented in previous sections [see Eq. (1)] using average fidelity [98]. Average fidelity is a measure of how well a certain process implements a desired operation. In our case, the process is the time evolution of the circuit and the operation we compare this with is the time evolution according to the target Hamiltonian. The average is over all possible initial states.

A. The circuit

The circuit can be seen in Fig. 7(a). It consists of four all-to-all connected nodes, and we may divide the branches in two groups. The blue and red branches have the same circuit elements but each their own circuit parameters. They will be shown to each implement a spin representing a matter field. The purple branches likewise have the same circuit elements, with identical parameters, and they connect the blue and red branches to each other. These branches will altogether implement a spin representing a gauge link. A similar circuit was designed and experimentally tested in Ref. [99] to realize a qubit with a very long lifetime. Each node in our circuit has been coupled capacitively to ground via an identical capacitance K. Ideally this capacitance is zero but has been included to study the effects of coupling to ground as well as capacitive coupling to control or readout devices. There are four external fluxes, Φ_i for $i = 1, 2, 3, 4$, threaded through loops, each consisting of two Josephson junctions in parallel, in the purple branches. The Josephson junctions themselves are imagined to be implemented with superconducting quantum interference devices (SQUIDs) such that the Josephson energy of each has an increased interval of possible values and high tunability. In Fig. 7(b), the layout of the circuit is chosen such that the Φ_i only pass through the circuit loops with the Josephson junctions pertaining to E_s, using air bridges [100–105], and the modular scalability of the circuit has also been made explicit. The idea is to make copies of the circuit in sequence, while using the same branches for the matter site spins. If the circuit parameters are chosen with the same symmetries as in Fig. 7(a), the eigenmodes of the capacitance network will not be affected by the additional copies. The shared branch of two connected blocks will precisely represent a matter connected
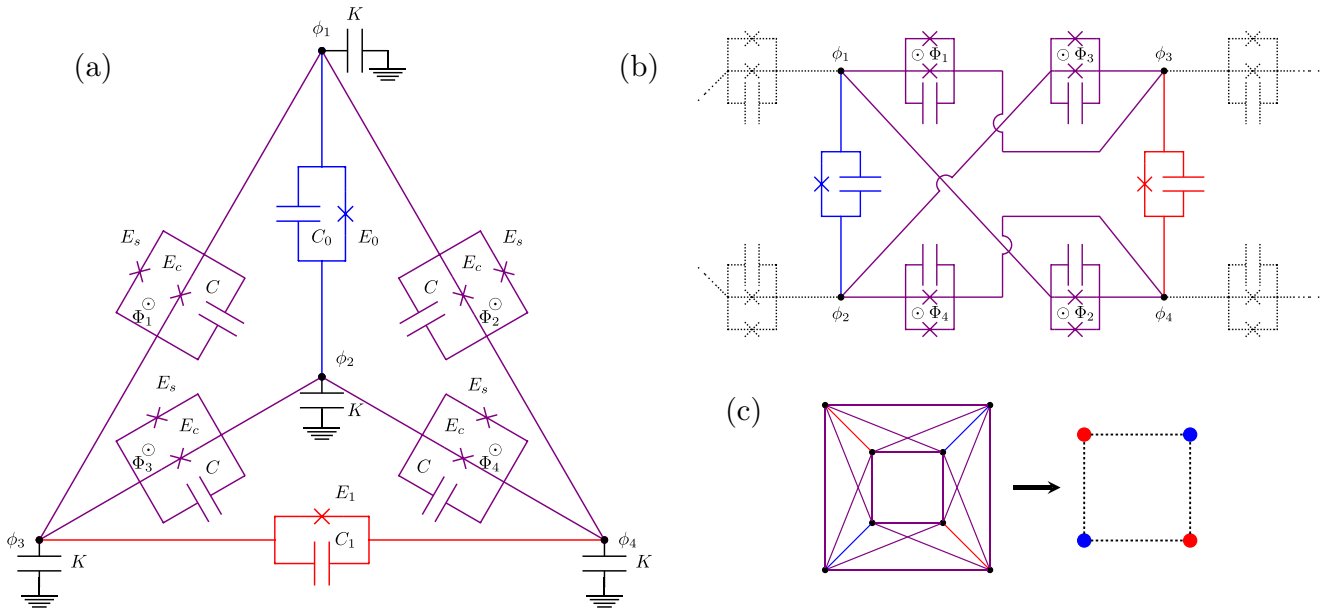
FIG. 7. (a) The diagram of the circuit used to implement three spins interacting via a direct three-body XXX coupling. Notice the identical circuit parameters. The identical grounding of each node has been included only for completeness of the study. We implement the spins via the eigenmodes of the capacitive network. The branches pertaining to each of these modes have been colored separately. The blue and red branches will implement matter sites spins, while the purple branches implement the gauge link spin. (b) The same circuit but now folded to make the modular scalability of the circuit completely clear. Multiple copies of the circuit, sharing the matter site branches pairwise, will implement a chain of matter sites coupled via gauge links. (c) A simple diagram of how four copies of the circuit could be put together to implement the periodic $N = 4$ version of Eq. (1).

to two gauge links, and only the desired interactions will be present. The circuit can thus be quite intuitively scaled to a chain of matter sites interacting through gauge links. A matter site branch could potentially also be shared by more than two copies of the circuit, making it possible to realize more complicated configurations. This would, however, result in many wires connecting to the same branch and require many bridges. The ability to cross conductors via air bridges makes SQCs a suitable platform to implement periodic boundary conditions. Bridges make it possible to access all points in a complicated circuit, while keeping it planar. In order to simulate the periodic system considered in the first part of this paper for the simplest interesting case, i.e., $N = 4$, we would have four copies of the circuit put together in this way, forming a square. A simple diagram of such a circuit and the resulting spin system can be seen in Fig. 7(c). In Sec. VII, we will consider readout of the circuit by dispersively coupling resonators to just the matter site branches; i.e., readout of the square would be done by coupling resonators to its corner branches.

B. Hamiltonian

In the following, we will consider only a single copy of the circuit. If we put several together to form a square or some larger system, the circuit parameters would have to be retuned. However, only the spin model parameters of the modes on the branches which are shared with the new copies will be affected by them, i.e., the matter field modes. These do, however, have their own circuit parameters, which affect only the matter modes. These are the parameters with a subscript

in Fig. 7(a) on the red and blue branches. Hence, the effect of the new copies could be compensated for by changing these parameters correspondingly.

We define the node fluxes of the circuit $\boldsymbol{\phi} = (\phi_1, \phi_2, \phi_3, \phi_4)^T$ [66] but will be working in the eigenmodes of the capacitive network [62–65,106], $\boldsymbol{\psi} = (\psi_{CM}, \psi_0, \psi_g, \psi_1)^T$, defined through

$$\boldsymbol{\phi} = \begin{pmatrix} 1 & 1 & \frac{1}{2} & 0 \\ 1 & -1 & \frac{1}{2} & 0 \\ 1 & 0 & -\frac{1}{2} & 1 \\ 1 & 0 & -\frac{1}{2} & -1 \end{pmatrix} \boldsymbol{\psi}.$$

This results in no interactions through the capacitors, greatly reducing the complexity of the interactions in the system. We will se how the modes ψ_0 and ψ_1 will represent two matter sites, and ψ_g will represent the gauge link between them. We will furthermore introduce a new set of external fluxes, Ψ_0, Ψ_g, and Ψ_1, of which the Φ_i are certain simple, linear combinations. We set these external fluxes to be constant $\Psi_j = -\pi/2$ for $j = 0, g, 1$. For details on the external fluxes and the derivation of the Hamiltonian, see the Supplemental Material [67]. In these coordinates and with these choices of external fluxes, the circuit Hamiltonian becomes

$$
\begin{aligned}
H_c = {} & \frac{\mathcal{K}_{00}^{-1}}{2} q_0^2 + \frac{\mathcal{K}_{gg}^{-1}}{2} q_g^2 + \frac{\mathcal{K}_{11}^{-1}}{2} q_1^2 \\
& - E_0 \cos \psi_0 - E_1 \cos \psi_1 \\
& - 4 E_c \cos \psi_0 \cos \psi_g \cos \psi_1 \\
& - 4 E_s \sin \psi_0 \sin \psi_g \sin \psi_1,
\end{aligned}
\tag{3}
$$

where q_j are momentum variables conjugate to the ψ_j, and $\mathcal{K}_{jj}^{-1}$ are the diagonal entries of the inverse capacitance matrix in the basis of the ψ_j coordinates. This Hamiltonian describes three transmon-like [107] anharmonic oscillator modes, interacting only through the interesting triple cosine and sine interactions. These are direct, completely even, and completely odd three-body interactions, respectively. The sine functions come about as a consequence of setting $\Psi_j = -\pi/2$. Recasting each of the ψ_j and q_j variables in terms of harmonic oscillator operators, i.e., bosonic creation and annihilation operators, $a_j^\dagger$ and a_j, and truncating the system to the two lowest levels of each yield the following spin Hamiltonian:

$$
\begin{aligned}
H_s = &-\tfrac{1}{2}\Omega_0\sigma_0^z - \tfrac{1}{2}\Omega_g\sigma_g^z - \tfrac{1}{2}\Omega_1\sigma_1^z \\
&+ J_{0g}^z\sigma_0^z\sigma_g^z + J_{01}^z\sigma_0^z\sigma_1^z + J_{g1}^z\sigma_g^z\sigma_1^z \\
&+ J_{0g1}^z\sigma_0^z\sigma_g^z\sigma_1^z + J_{0g1}^x\sigma_0^x\sigma_g^x\sigma_1^x,
\end{aligned} \quad (4)
$$

where the Ω's and J's are spin model parameters. To calculate the parameters, we use a method introduced by the authors in Ref. [106], which avoids approximating the trigonometric functions via a Taylor expansion but instead takes their full effect into account. This gives more accurate parameters, when truncating the flux Hamiltonian, and can be used for any sine or cosine of a linear combination of the flux coordinates. The exact dependence of the spin model parameters on the circuit parameters and details on their derivation can be seen in the Supplemental Material [67]. However, we note that the XXX-coupling strength is proportional to E_s, and E_s does not appear anywhere else in the spin model parameters, making the XXX coupling separately tunable. The circuit has thus resulted in three spins interacting through several Z-type couplings, and a direct XXX coupling. As we detail below, the XXX coupling can be tuned to $\sigma_0^+\sigma_g^+\sigma_1^- +$ H.c., which is exactly the U(1) gauge coupling in Eq. (1), $\sigma_0^+S_{0,1}^+\sigma_1^- +$ H.c. This shows how the ψ_0 and ψ_1 modes will represent matter site spins, while the ψ_g mode has the role of gauge link spin. The circuit could be simplified a great deal, by removing the E_c junctions, which would seemingly not disturb any of the desired terms in the Hamiltonian. However, this is not quite true, as the triple cosine term is the only source of anharmonicity for the ψ_g mode. The anharmonicities α_j of the three modes, which justify the truncation to the two lowest level of each anharmonic oscillator, can be seen in the Supplemental Material [67].

C. Higher levels

Let us briefly consider the effect of interactions between the spin-1/2 subspace and the higher levels of the circuit. There will generally be even interactions like $a_j^\dagger a_j^\dagger a_{j'} a_{j'} +$ H.c. or $a_j^\dagger a_j^\dagger a_j^\dagger a_{j'}^\dagger +$ H.c., where there is an even number of creation and annihilation operators for each mode, as well as odd interactions where there is an odd number of creation and annihilation operators. The even interactions will generally be suppressed if their coupling strengths are much smaller than the spin transition energies, while the odd interactions will generally be suppressed if their coupling strengths are much smaller than the anharmonicities. As J^z and J_{0g1}^x represent the

coupling strengths of higher order even and odd couplings respectively, this means that we must have $J^z \ll \Omega_j$ and $J_{0g1}^x \ll \alpha_j$ in our system. However, even in this regime, where the dynamics mainly take place in the spin-1/2 subspace, there will still be the important question of the exact effect of the higher levels in the anharmonic oscillator degrees of freedom, both for effective interactions and leakage [63,106–114]. Below we will include higher levels in our numerics to judge the impact directly and show the regimes necessary to reduce these effects. In particular, the system will undergo virtual excitations and de-excitations, which effectively renormalize the spin model parameters. This results in having to tune effective parameters and not the explicit ones which appear in Eq. (4). This is what we have done numerically, and we will discuss it in detail in the next section.

D. Connecting to the QLM Hamiltonian

In order to achieve a staggered mass for the matter site spins, and no mass for the gauge link spin, we use an approach from Ref. [70]. Let $H_s = H_0 + H_{\text{int}}$, where H_0 contains all the Z-type terms and H_{int} is just the XXX coupling. Consider then H_s in a frame rotating with respect to $H_m = H_0 + \tfrac{1}{2}m(\sigma_0^z - \sigma_1^z)$:

$$
\begin{aligned}
H_R &= e^{iH_m t}[H_s - H_m]e^{-iH_m t} \\
&= -\tfrac{1}{2}m\sigma_0^z + \tfrac{1}{2}m\sigma_1^z + J_{0g1}^x \sum_{p,r,s \in \{+,-\}} e^{-i\omega_{prs}t}\sigma_0^p\sigma_g^r\sigma_1^s,
\end{aligned} \quad (5)
$$

where the sum is over all eight combinations of the three $\sigma_i^\pm$ and the frequency of their phase is given by

$$
\omega_{prs} = p(\Omega_0 - m) + r\Omega_g + s(\Omega_1 + m) + 2prsJ_{0g1}^z.
$$

If the system is now to tuned such that for example $\omega_{++-} = -\omega_{--+} = 0$, then the operator $\sigma_0^+\sigma_g^+\sigma_1^- +$ H.c. will be resonant, as desired. All other combinations will be off resonant and would disappear in a RWA, as long as the spin transition frequencies and their differences are much larger than the J^z, which is already something we must fulfill to justify the truncation to the spin-$\tfrac{1}{2}$ subspace. Furthermore, we have recovered the staggered mass of Eq. (1) via the terms $-\tfrac{1}{2}m\sigma_0^z + \tfrac{1}{2}m\sigma_1^z$. Thus, in an appropriately rotating frame, the Hamiltonian in Eq. (4) implemented by the circuit indeed recreates the one-dimensional U(1) quantum link model of Eq. (1) for two matter sites and the link between them.

The circuit design principles we have used here, i.e., looking at the eigenmodes of the capacitive network in a symmetric circuit to achieve multibody couplings and suppressing as many undesired interactions as possible, could be used to achieve other interesting gauge-invariant systems. It would be an obvious next step to work toward higher gauge symmetries, like SU(2), or to attempt to implement gauge link operators with three levels. The latter would allow for the study of confinement and might be implemented by using two spin-1/2's to represent one gauge field.

VI. OPTIMIZING CIRCUIT PARAMETERS AND AVERAGE FIDELITY

A. Initial considerations

We now go through some considerations necessary for the optimization of circuit parameters. As mentioned, higher order contributions from interactions with states outside the spin-$\frac{1}{2}$ subspace mean that we must consider effective spin model parameters when optimizing the circuit parameters. We are in particular interested in the effective detuning, Δ_{eff}, between $|\uparrow_0 \uparrow_g \downarrow_1\rangle$ and $|\downarrow_0 \downarrow_g \uparrow_1\rangle$ (with $\downarrow_i$ and $\uparrow_i$ referring to the ground and excited states of the ith spin) corresponding to ω_{++-} in the above, and the effective coupling strength, J_{eff}, of the XXX coupling corresponding to J_{0g1}^x in the above. Furthermore, we want the numerical value of the anharmonicities of the modes to be about $100 \times 2\pi$ MHz or larger [108]. For details on how to numerically determine Δ_{eff} and J_{eff}, see the Supplemental Material [67]. We want to show that this circuit can be used to realize the quench dynamics studied in the first part of this paper. In this case, the effective detuning should not be zero, but rather it defines the staggered mass m. Considering the rotated Hamiltonian H_R in Eq. (5), it can be seen that we get the desired mass term when $\Delta_{\text{eff}} = 2m$. Likewise, if J is the desired strength of the matter-gauge coupling in Eq. (1), then we must have $J_{\text{eff}} = J/2$, because of the factor $1/2$ in the interaction term in Eq. (1). We will thus be tuning $J/m = 4J_{\text{eff}}/\Delta_{\text{eff}}$.

Since only the Josephson energies of a SQC can be tuned *in situ*, it is difficult to actually perform the appropriate quench of the circuit. Instead, we intend for the circuit to be constructed with the postquench parameters. The quench will then be implemented by initializing the system in the ground state of the prequench Hamiltonian. Whether we have the system in its prequench setup, go into its ground state, and then quench to the postsetup, or simply start with the system in the postquench setup and then quickly initialize in the ground state of the prequench Hamiltonian, we will see the same resulting dynamics. This moves the difficulty from performing a fast quench to performing a fast initialization.

B. Optimizing with respect to average fidelity

With all this in mind, we tune the circuit parameters to yield a negative J/m (as the quench is to a negative mass, $m \to -m$), corresponding to postquench parameters. After finding appropriate circuit parameters, we do a check of the overall behavior of the circuit, ensuring that it works as intended, including no disturbing interactions with higher levels. To do this, we use average fidelity [98]. As mentioned, average fidelity is a measure of how well a certain process implements a desired operation. It is calculated as the fidelity of the process implementation of the operation, averaged over initial states. In our case, the process is the time evolution of the circuit, determined by H_c in Eq. (3), in a frame rotating such that the resulting Hamiltonian is H_R in Eq. (5), where m is set to $\Delta_{\text{eff}}/2$ and the bare coupling strength J_{0g1}^x is replaced with J_{eff}. To take contributions from higher level interactions into account, we truncate to the lowest four levels. We only rotate the spin-$1/2$ states; i.e., we use a four-level version of $H_0 + \frac{1}{2}m(\sigma_0 - \sigma_1)$, where all entries pertaining to levels

higher than the spin-$1/2$ states are just zero. Furthermore, we must use an effective version of H_0, where contributions to the energy levels from virtual interactions are included. In an experimental setting, this $H_{0,\text{eff}}$ could be determined in a separately, by setting $E_s = 0$ via flux tuning, thus turning off the XXX coupling and then initializing in each of the spin-$1/2$ states, which would then be very close to eigenstates of the system, such that their phase over time would yield their effective energy.

The operation we compare this with is the time evolution according to the target Hamiltonian, i.e., H from Eq. (1) with two matter sites and a gauge link between them. We compare only the dynamics of the spin-$1/2$ states; i.e., time evolution of the circuit takes place with four levels included for each mode, and the result is then projected down to the spin-$1/2$ subspace, before comparison with the time evolution of H. For details on how the average fidelity is calculated, see the Supplemental Material [67].

The average fidelity will thus be comparing the very time evolution operators themselves for the circuit and the target system. The mass and coupling strength of the target Hamiltonian are chosen to be $\Delta_{\text{eff}}/2$ and $2J_{\text{eff}}$. The fidelity would thus *a priori* be expected to be quite high, but since this is all done with four levels included in each anharmonic mode, the fidelity will be a measure of how much the higher levels affect the dynamics of the circuit beyond just the renormalization of the mass and coupling strength. In particular, some population will be lost to the higher levels, and just as virtual processes contribute to the strength of the XXX coupling, they will also to some extent induce other effective interactions. These will disturb the desired dynamics and might be gauge variant, resulting in population moving outside of the $G_n = 0$ gauge sector of the spin-$1/2$ subspace.

C. Result

In the Supplemental Material [67], we show an example of a realistic set of circuit parameters satisfying our demands, yielding $J/m = 4J_{\text{eff}}/\Delta_{\text{eff}} = -2.0$, which according to Figs. 5 and 6 would result in interesting dynamics of the order parameter and Loschmidt amplitude within a time of $tm = 2$, corresponding here to $t = 49.5$ ns (remember that we optimize for postquench J/m, i.e., negative values, while Figs. 5 and 6 show prequench values of J/m). In our work with tuning the circuit, we have found that it is well capable of implementing the interval of J/m considered in the first part of this paper. If a circuit is made that implements an interesting value of J/m, other nearby values could be achieved by varying just the Josephson energies, making it possible to use the same circuit to study different values of J/m.

All calculations of dynamics are performed without including noise. The effect of different types of noise in analog simulation of LGTs and how to suppress it has already been studied extensively [44,115–121]. Our results here instead highlight the basic high quality of the presented circuit implementation of a QLM. Furthermore, with present superconducting qubit lifetimes [99,122,123], we do not believe noise would significantly disturb the results presented here. While we have explained how the XXX coupling in a RWA yields the desired U(1) interaction term, we do not actually
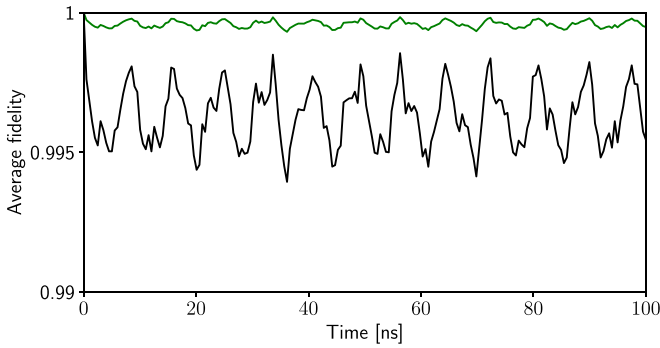
FIG. 8. In black: The average fidelity of the circuit's implementation of the target dynamics in a rotating frame. The fidelities are close to or above 99.5% and keep steady over long times, with an oscillation on a short timescale. In green: The fidelity without taking leakage to the higher levels into account. From this, we see that the largest part, 0.2–0.45%, of the lost fidelity is due to population immediately leaking into the higher levels and then partly oscillating back and forth. A smaller contribution, about 0.05%, is from the effective interactions induced by virtual processes involving the higher levels.

use the resulting approximate Hamiltonian in our numerics but instead retain all terms to show directly that they do indeed not disturb the desired dynamics significantly. In Fig. 8, the calculated average fidelity of the circuit's implementation of the target dynamics using the circuit parameters presented in the Supplemental Material [67] can be seen in black. The fidelity is about or above 99.5% at all times, and while it oscillates on a short timescale, it seems to keep steady over the plotted interval. Hence, the implementation of the desired dynamics is good, and stable in the sense that we are not accumulating error or continuously losing population to the higher levels. We seem to lose a small fraction of the population immediately, which then partly oscillates back and forth. The same average fidelity plus the leakage to higher levels is plotted in green; i.e., this plot shows the fidelity if we do not take leakage into account. Hence, we can see that about 0.2–0.45% fidelity is lost because of population leaking to the higher levels of the circuit, while about 0.05% is lost due to effective interactions induced by virtual processes involving the higher levels. These high and steady fidelities show directly how our superconducting circuit truly implements the desired dynamics, with circuit parameters available to experiments. Hence, the circuit is a strong candidate for studying the U(1) QLM with present NISQ-era devices.

VII. READOUT FOR STATE TOMOGRAPHY

A. Reading out $\mathcal{G}(t)$ and $g(k, t)$

An important thing to note is that the Loschmidt amplitude in the circuit's own frame will not be the same as in the rotating frame. This is because under unitary transformations like $e^{-iH_c t} \rightarrow U e^{-iH_c t}$, where the operators are simultaneously transformed as $A \rightarrow U A U^\dagger$, quantities like $\mathcal{G}(t) = \langle \psi(0)|e^{-iH_c t}|\psi(0)\rangle$ or the order parameter $g(k, t) = \langle \psi(0)|\mathfrak{g}(k)e^{-iH_c t}|\psi(0)\rangle$ get an odd number of U operators. Hence, these operators cannot cancel and the quantities are not

invariant. The Loschmidt amplitude and our order parameter are therefore not invariant under rotations like the one we performed to find H_R. However, the Loschmidt amplitude is often measured by performing state tomography [124–128] and then calculating $\mathcal{G}(t)$ from the results [21,24–27,34]. With full information about the state of the circuit at any time, the Loschmidt amplitude can easily be calculated.

B. Dispersive readout of coupled qubits

To perform readout of the circuit, we would use a method inspired by Refs. [64,65]. Here they perform quantum state tomography of two qubits by measuring the dispersive shift of a resonator coupled to just one of them. The idea is that strong ZZ couplings shift the energy of one qubit conditioned on the state of the other sufficiently such that it can be seen in the dispersive shift of the resonator. Hence, where normally one observes two shifts of the resonator corresponding to the two eigenvalues of σ^z, one would see four shifts corresponding to the four combinations of eigenvalues from the two qubits. Single-qubit rotations are used to measure the qubits along their x and y axes allowing for full state tomography. For details, see Refs. [64,65] and their Supplemental Materials. Similarly, here we imagine doing readout of just the matter site spins. A resonator coupled through identical capacitors to the two nodes pertaining to a matter site mode will couple to just that mode. Hence, usual dispersive readout of the spin can be performed. The ZZ couplings between this mode and its neighboring gauge and matter modes will make it possible to derive some information about them as well. In particular, we want to extract information about the gauge modes by coupling to just the matter modes. It is easier to couple to the matter modes, as they live on a single branch between two nodes, while the gauge modes live on four branches between four nodes. We therefore propose measuring on all matter modes and comparing the data to extract information about the whole system. For a single module of our circuit, measurements on either of the matter modes give information on both matter modes and the gauge mode between them. For a 1D chain of modules, measurement on a matter mode would give information on that matter mode and the two matter modes and the two gauge modes to which it is coupled.

C. Effective dispersive shifts

We now consider the shifts one would measure for a single module of our circuit. The effective resonance frequency of a resonator dispersively coupled to a qubit is [107]

$$\omega_r' = \omega_r - \frac{g_r^2}{\Delta + \alpha} - \left(\frac{g_r^2}{\Delta} - \frac{g_r^2}{\Delta + \alpha}\right)\sigma^z. \qquad (6)$$

Here ω_r is the bare resonance frequency, σ_z pertains to the qubit, $\Delta = \omega_q - \omega_r$ is the detuning between the transition frequency ω_q of the qubit and ω_r, α is the anharmonicity of the qubit, and finally g_r is the strength of the dispersive coupling. Here σ_z is not to be understood as an operator, but the appropriate eigenvalue of the state that the qubit has collapsed to. The transition frequency ω_q is in our case a combination of the bare spin transition frequency and ZZ-coupling strengths. If we consider coupling a resonator to spin 0 in H_s of Eq. (4),
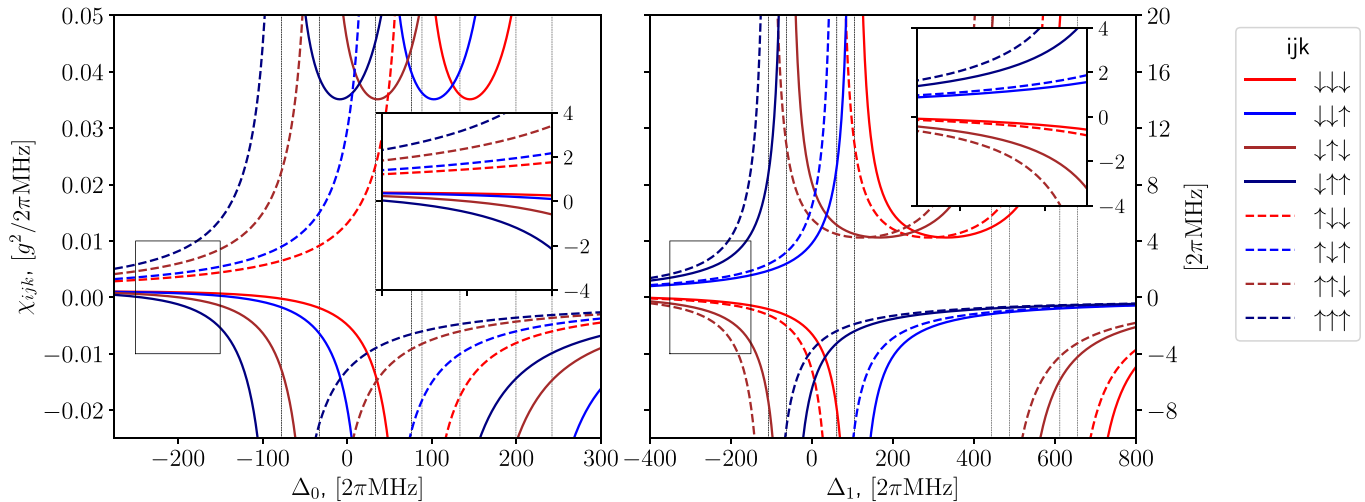
FIG. 9. Left and right, the shift χ_{ijk} of the resonance frequency of a resonator dispersively coupled to spin 0 or spin 1, respectively, for all eight spin-1/2 states of the circuit. The shifts are plotted as functions of the bare detuning $\Delta_n = \Omega_n - \omega_r$ for $n = 0, 1$ respectively. The indices $ijk = \downarrow, \uparrow$ denote the state of each of the three spins. Assuming a resonator coupling strength of $g_r = 20 \times 2\pi$ MHz, we get the energy scale shown on the right y axis. The insets show intervals of the bare detunings where the dispersive shifts of each state are distinct enough to distinguish between the eight spin state with just these two measurements, particularly when the information from each measurement is compared. To be in the dispersive regime, we must have $\chi_{ijk} \ll g_r$; i.e., we must stay well away from the points where χ_{ijk} diverges, which are marked with vertical dashed lines.

then we can see that

$$\omega_q = \Omega_0 - 2\left(J_{0g}^z \sigma_g^z + J_{01}^z \sigma_1^z + J_{0g1}^z \sigma_g^z \sigma_1^z\right)$$

where the operators, like the σ^z in Eq. (6), are to be understood as some specific eigenvalue corresponding to the state of the circuit, which has collapsed as we measured it. We can now consider the dispersive shift $\chi_{ijk} = \omega_r' - \omega_r$ of the resonator frequency as a function of the bare detuning $\Delta_0 = \Omega_0 - \omega_r$, where $i, j, k = \downarrow, \uparrow$ refers to whether spin 0, g, 1, respectively, has collapsed to $|\downarrow\rangle$ or $|\uparrow\rangle$. In Fig. 9, the eight shifts, corresponding to the eight spin-1/2 states of the circuit, for both coupling to spin 0 and 1 are plotted, using the same circuit parameters is in our previous plots. We now want to find values of Δ_0 and Δ_1 such that the eight shifts are as distinct as possible, and where comparing shifts from both of the spins helps to determine the state of the gauge link spin. In order to remain in the dispersive region, we must satisfy $g_r/|\Delta|, g_r/|\Delta + \alpha| \ll 1$, where Δ now has a different value for each of the spin-1/2 states. Looking at Eq. (6), we can see that $\chi_{ijk} \sim g_r^2/|\Delta|, g_r^2/|\Delta + \alpha|$, and thus the conditions for the dispersive regime can be written as $\chi_{ijk} \ll g_r$. This essentially means we must stay well away from the regions where χ_{ijk} diverges. These are marked with vertical dashed lines in Fig. 9. If for the sake of example we consider a resonator coupling strength of $g_r = 20 \times 2\pi$ MHz, we get the energy scale shown on the right y axis of Fig. 9. In the insets of Fig. 9 can be seen enlargements of the regions between $\chi_{ijk} = \pm 4 \times 2\pi$ MHz. If we choose a bare detuning within these regions, we could use the shift of the first resonator (the left inset) to distinguish between the dashed and solid lines, i.e., the state of spin 0, and use the second resonator (the right inset) to distinguish between the blue-navy and the red-brown lines, i.e., the state of spin 1. This is similar to dispersive measurement of qubits, but we can further use this information to distinguish between the shifts caused by

the state of the gauge link spin, g. With a resolution of $1 \times 2\pi$ MHz in a measurement of the dispersive shift, which is experimentally feasible [25,64,65,129], it would be possible to distinguish the states of the circuit with this or even a smaller choice of g_r.

The above analysis is approximate, as it uses only the bare spin model parameters, and the formula Eq. (6) is derived for a single qubit with some specific bare transition frequency coupled to a resonator. In our case, it is clear that the higher levels of the circuit would affect these calculations, and it is in fact a resonator, or several, coupled to the circuit, a system of multiple interacting qubits or spins. A more accurate analysis using numerical methods could be carried out to find the actual shifts of the resonance frequency of the resonator dependent on the circuit state. However, the quantitative results would be the same, namely that the different states would result in different shifts. It would then be a matter of determining whether those shifts would be sufficient to distinguish the states in a measurement, using the comparative method outlined above. Whether or not this is the case is in the end a consequence of the chosen circuit parameters, so one could optimize the circuit parameters with respect to these considerations in addition to the conditions we outlined previously. These dispersive readouts could then be used to perform a full quantum state tomography, yielding all information about the Loschmidt amplitude or the order parameter we introduced in the first part of this paper.

An alternative to performing full state tomography is to have multiple copies of the circuit and to perform the quench experiment in just one of them while initializing the other in the appropriate initial state. The circuits are then connected using some appropriate scheme to make their states interfere, potentially yielding information about the quantities we are interested in. Such an approach is used in the context of atoms in an optical lattice in Refs. [130,131] to measure the

Rényi entropy. This has in fact been experimentally probed [132–134].

VIII. CONCLUSION

We have shown how to realize lattice gauge theories through quantum link models in superconducting quantum circuits. Specifically, we have provided a method for general circuits to implement quantum link models with a high average fidelity. This opens up the possibility for experimental study of quantum link models in NISQ-era devices. As a demonstration of the principles in our work, we have studied a periodic $(1+1)$D spin-1/2 quantum link model with local U(1) gauge symmetry, corresponding to the Schwinger model in the continuum. Even with the smallest lattice considered, the system undergoes dynamical quantum phase transitions after a quench of the sign of the mass. With this in mind, we have proposed a superconducting circuit, which realizes three spin-1/2's interacting via a direct XXX coupling, which through appropriate tuning becomes the matter-gauge interaction necessary for a U(1) quantum link model. The circuit can be modularly scaled in an intuitive way and for a single module of the circuit realizes the desired U(1) QLM dynamics with an average fidelity of about 99.5% or above, using realistic circuit parameters. From this, we expect that the dynamical quantum phase transitions we have found should be observable in an experimental realization of the circuit.

We studied an order parameter, which is essentially the Fourier transform of the gauge-invariant string order parameters connecting a representative particle and antiparticle site to all other sites of the system. This order parameter had zeros that correlated with the minima of the Loschmidt amplitude and its zeros. The zeros of both the Loschmidt amplitude and our complex order parameter were found by looking for vortices in their phases. These vortices, which appear exactly when the function goes to zero, are much easier to find numerically, as they are extended structures, and their center point can be found by looking at the line of discontinuity, which extends from it. The vortices are topological in nature; in particular, they can be counted by a winding number which then constitutes a dynamical topological order parameter of the

system. The vortices of the order parameter showed dynamics of creation and annihilation. We found that the structure of the Loschmidt amplitude, as well as its zeros in the parameter space of matter-gauge coupling strength and time, quickly converges to a certain pattern, with the zeros lying along lines. Hence, even the smallest system size considered would reveal the tendencies of the larger systems in an experimental realization. Finally, we considered readout of the circuit, using a method of resonators coupled dispersively to a subset of the circuit spins, but which nonetheless gave information about all the spins, by exploiting their pairwise ZZ couplings. To use this in the context of the quench dynamics we have studied, we imagine that quantum state tomography of the circuit is performed to extract the data necessary to calculate the Loschmidt amplitude and our order parameter.

In future work, it would be interesting to study dynamics of more complicated lattice configurations and gauge theories. For example, periodic 2D (i.e., toric) QLMs could be considered, which would likely show interesting topological aspects. Additional degrees of freedom could be added to the link operators; indeed simply promoting them to spin-1's would allow for the study of confinement and pair production. It would be natural to work toward a superconducting circuit realization of such models using the same design principles we have presented here. A similarly modular circuit realizing SU(2) symmetric interactions between fermions or some other interesting gauge symmetry like $\mathbb{Z}_n$ would be interesting to develop. Further work could also be done on the specific system studied here. It would be interesting to link the dynamical quantum phase transitions found here to a potential underlying equilibrium phase transition or entropy production [19,21,24].

[1] I. M. Georgescu, S. Ashhab, and F. Nori, Quantum simulation, Rev. Mod. Phys. **86**, 153 (2014).

[2] J. Zhang, P. W. Hess, A. Kyprianidis, P. Becker, A. Lee, J. Smith, G. Pagano, I.-D. Potirniche, A. C. Potter, A. Vishwanath, N. Y. Yao, and C. Monroe, Observation of a discrete time crystal, Nature (London) **543**, 217 (2017).

[3] S. Choi, J. Choi, R. Landig, G. Kucsko, H. Zhou, J. Isoya, F. Jelezko, S. Onoda, H. Sumiya, V. Khemani, C. von Keyserlingk, N. Y. Yao, E. Demler, and M. D. Lukin, Observation of discrete time-crystalline order in a disordered dipolar many-body system, Nature (London) **543**, 221 (2017).

[4] M. Schreiber, S. S. Hodgman, P. Bordia, H. P. Luschen, M. H. Fischer, R. Vosk, E. Altman, U. Schneider, and I. Bloch, Observation of many-body localization of interacting fermions in a quasirandom optical lattice, Science **349**, 842 (2015).

[5] J. Smith, A. Lee, P. Richerme, B. Neyenhuis, P. W. Hess, P. Hauke, M. Heyl, D. A. Huse, and C. Monroe, Many-body localization in a quantum simulator with programmable random disorder, Nat. Phys. **12**, 907 (2016).

[6] M. Gring, M. Kuhnert, T. Langen, T. Kitagawa, B. Rauer, M. Schreitl, I. Mazets, D. A. Smith, E. Demler, and J. Schmiedmayer, Relaxation and prethermalization in an isolated quantum system, Science **337**, 1318 (2012).

[7] B. Neyenhuis, J. Zhang, P. W. Hess, J. Smith, A. C. Lee, P. Richerme, Z.-X. Gong, A. V. Gorshkov, and C. Monroe, Observation of prethermalization in long-range interacting spin chains, Sci. Adv. **3**, e1700672 (2017).

[8] C. Neill, P. Roushan, M. Fang, Y. Chen, M. Kolodrubetz, Z. Chen, A. Megrant, R. Barends, B. Campbell, B. Chiaro, A. Dunsworth, E. Jeffrey, J. Kelly, J. Mutus, P. J. J. O'Malley, C.

Quintana, D. Sank, A. Vainsencher, J. Wenner, T. C. White, et al., Ergodic dynamics and thermalization in an isolated quantum system, Nat. Phys. **12**, 1037 (2016).

[9] E. A. Martinez, C. A. Muschik, P. Schindler, D. Nigg, A. Erhard, M. Heyl, P. Hauke, M. Dalmonte, T. Monz, P. Zoller, and R. Blatt, Real-time dynamics of lattice gauge theories with a few-qubit quantum computer, Nature (London) **534**, 516 (2016).

[10] M. Heyl, A. Polkovnikov, and S. Kehrein, Dynamical Quantum Phase Transitions in the Transverse-Field Ising Model, Phys. Rev. Lett. **110**, 135704 (2013).

[11] M. Heyl, Scaling and Universality at Dynamical Quantum Phase Transitions, Phys. Rev. Lett. **115**, 140602 (2015).

[12] E. Canovi, P. Werner, and M. Eckstein, First-Order Dynamical Phase Transitions, Phys. Rev. Lett. **113**, 265702 (2014).

[13] D. Pekker, G. Refael, E. Altman, E. Demler, and V. Oganesyan, Hilbert-Glass Transition: New Universality of Temperature-Tuned Many-Body Dynamical Quantum Criticality, Phys. Rev. X **4**, 011052 (2014).

[14] R. Vosk and E. Altman, Dynamical Quantum Phase Transitions in Random Spin Chains, Phys. Rev. Lett. **112**, 217204 (2014).

[15] M. Schmitt and S. Kehrein, Dynamical quantum phase transitions in the Kitaev honeycomb model, Phys. Rev. B **92**, 075114 (2015).

[16] A. A. Zvyagin, Nonequilibrium dynamics of a system with two kinds of fermions after a pulse, Phys. Rev. B **95**, 075122 (2017).

[17] Y.-P. Huang, D. Banerjee, and M. Heyl, Dynamical Quantum Phase Transitions in U(1) Quantum Link Models, Phys. Rev. Lett. **122**, 250401 (2019).

[18] M. Lacki and M. Heyl, Dynamical quantum phase transitions in collapse and revival oscillations of a quenched superfluid, Phys. Rev. B **99**, 121107(R) (2019).

[19] B. O. Goes, G. T. Landi, E. Solano, M. Sanz, and L. C. Céleri, Wehrl entropy production rate across a dynamical quantum phase transition, Phys. Rev. Res. **2**, 033419 (2020).

[20] A. A. Zvyagin, Dynamical quantum phase transitions, Low Temp. Phys. **42**, 971 (2016).

[21] M. Heyl, Dynamical quantum phase transitions: A review, Rep. Prog. Phys. **81**, 054001 (2018).

[22] M. Heyl, Dynamical quantum phase transitions: A brief survey, EPL **125**, 25 (2019).

[23] S. Sachdev, *Quantum Phase Transitions*, 2nd ed. (Cambridge University Press, Cambridge, UK, 2011).

[24] P. Jurcevic, H. Shen, P. Hauke, C. Maier, T. Brydges, C. Hempel, B. P. Lanyon, M. Heyl, R. Blatt, and C. F. Roos, Direct Observation of Dynamical Quantum Phase Transitions in an Interacting Many-Body System, Phys. Rev. Lett. **119**, 080501 (2017).

[25] X.-Y. Guo, C. Yang, Y. Zeng, Y. Peng, H.-K. Li, H. Deng, Y.-R. Jin, S. Chen, D. Zheng, and H. Fan, Observation of a Dynamical Quantum Phase Transition by a Superconducting Qubit Simulation, Phys. Rev. Appl. **11**, 044080 (2019).

[26] K. Xu, Z.-H. Sun, W. Liu, Y.-R. Zhang, H. Li, H. Dong, W. Ren, P. Zhang, F. Nori, D. Zheng, H. Fan, and H. Wang, Probing dynamical phase transitions with a superconducting quantum simulator, Sci. Adv. **6**, eaba4935 (2020).

[27] X.-Y. Xu, Q.-Q. Wang, M. Heyl, J. C. Budich, W.-P. Pan, Z. Chen, M. Jan, K. Sun, J.-S. Xu, Y.-J. Han, C.-F. Li, and G.-C.

Guo, Measuring a dynamical topological order parameter in quantum walks, Light: Sci. Appl. **9**, 7 (2020).

[28] H. Hu and E. Zhao, Topological Invariants for Quantum Quench Dynamics from Unitary Evolution, Phys. Rev. Lett. **124**, 160402 (2020).

[29] S. Vajna and B. Dóra, Topological classification of dynamical phase transitions, Phys. Rev. B **91**, 155127 (2015).

[30] I. Hagymási, C. Hubig, Ö. Legeza, and U. Schollwöck, Dynamical Topological Quantum Phase Transitions in Nonintegrable Models, Phys. Rev. Lett. **122**, 250601 (2019).

[31] T. V. Zache, N. Mueller, J. T. Schneider, F. Jendrzejewski, J. Berges, and P. Hauke, Dynamical Topological Transitions in the Massive Schwinger Model with a θ Term, Phys. Rev. Lett. **122**, 050403 (2019).

[32] J. C. Budich and M. Heyl, Dynamical topological order parameters far from equilibrium, Phys. Rev. B **93**, 085416 (2016).

[33] C. Ding, Dynamical quantum phase transition from a critical quantum quench, Phys. Rev. B **102**, 060409(R) (2020).

[34] N. Fläschner, D. Vogel, M. Tarnowski, B. S. Rem, D.-S. Lühmann, M. Heyl, J. C. Budich, L. Mathey, K. Sengstock, and C. Weitenberg, Observation of dynamical vortices after quenches in a system with topology, Nat. Phys. **14**, 265 (2018).

[35] Z. Huang and A. V. Balatsky, Dynamical Quantum Phase Transitions: Role of Topological Nodes in Wave Function Overlaps, Phys. Rev. Lett. **117**, 086802 (2016).

[36] M. Fagotti, Dynamical phase transitions as properties of the stationary state: Analytic results after quantum quenches in the spin-1/2 XXZ chain, arXiv:1308.0277.

[37] S. Vajna and B. Dóra, Disentangling dynamical phase transitions from equilibrium phase transitions, Phys. Rev. B **89**, 161105(R) (2014).

[38] F. Andraschko and J. Sirker, Dynamical quantum phase transitions and the Loschmidt echo: A transfer matrix approach, Phys. Rev. B **89**, 125120 (2014).

[39] S. Porta, F. Cavaliere, M. Sassetti, and N. Traverso Ziani, Topological classification of dynamical quantum phase transitions in the xy chain, Sci. Rep. **10**, 12766 (2020).

[40] K. G. Wilson, Confinement of quarks, Phys. Rev. D **10**, 2445 (1974).

[41] J. Kogut and L. Susskind, Hamiltonian formulation of Wilson's lattice gauge theories, Phys. Rev. D **11**, 395 (1975).

[42] J. Smit, *Introduction to Quantum Fields on a Lattice*, Cambridge Lecture Notes in Physics (Cambridge University Press, Cambridge, UK, 2002), pp. 1–284.

[43] D. Banerjee, M. Dalmonte, M. Müller, E. Rico, P. Stebler, U.-J. Wiese, and P. Zoller, Atomic Quantum Simulation of Dynamical Gauge Fields Coupled to Fermionic Matter: From String Breaking to Evolution After a Quench, Phys. Rev. Lett. **109**, 175302 (2012).

[44] S. Kühn, J. I. Cirac, and M.-C. Bañuls, Quantum simulation of the Schwinger model: A study of feasibility, Phys. Rev. A **90**, 042305 (2014).

[45] Y. Kuno, K. Kasamatsu, Y. Takahashi, I. Ichinose, and T. Matsui, Real-time dynamics and proposal for feasible experiments of lattice gauge–Higgs model simulated by cold atoms, New J. Phys. **17**, 063005 (2015).

[46] V. Kasper, F. Hebenstreit, M. Oberthaler, and J. Berges, Schwinger pair production with ultracold atoms, Phys. Lett. B **760**, 742 (2016).

[47] A. S. Dehkharghani, E. Rico, N. T. Zinner, and A. Negretti, Quantum simulation of Abelian lattice gauge theories via state-dependent hopping, Phys. Rev. A **96**, 043611 (2017).

[48] Y. Kuno, S. Sakane, K. Kasamatsu, I. Ichinose, and T. Matsui, Quantum simulation of $(1+1)$-dimensional U(1) gauge–Higgs model on a lattice by cold Bose gases, Phys. Rev. D **95**, 094507 (2017).

[49] A. Mil, T. V. Zache, A. Hegde, A. Xia, R. P. Bhatt, M. K. Oberthaler, P. Hauke, J. Berges, and F. Jendrzejewski, A scalable realization of local U(1) gauge invariance in cold atomic mixtures, Science **367**, 1128 (2020).

[50] M. C. Bañuls, R. Blatt, J. Catani, A. Celi, J. I. Cirac, M. Dalmonte, L. Fallani, K. Jansen, M. Lewenstein, S. Montangero, C. A. Muschik, B. Reznik, E. Rico, L. Tagliacozzo, K. Van Acoleyen, F. Verstraete, U.-J. Wiese, M. Wingate, J. Zakrzewski, and P. Zoller, Simulating lattice gauge theories within quantum technologies, Eur. Phys. J. D **74**, 165 (2020).

[51] L. Sanchez-Palencia, Constructing field theories using quantum simulators, Physics **13**, 10 (2020).

[52] T. V. Zache, T. Schweigler, S. Erne, J. Schmiedmayer, and J. Berges, Extracting the Field Theory Description of a Quantum Many-Body System from Experimental Data, Phys. Rev. X **10**, 011020 (2020).

[53] B. Yang, H. Sun, R. Ott, H.-Y. Wang, T. V. Zache, J. C. Halimeh, Z.-S. Yuan, P. Hauke, and J.-W. Pan, Observation of gauge invariance in a 71-site Bose-Hubbard quantum simulator, Nature **587**, 392 (2020).

[54] D. Horn, Finite matrix models with continuous local gauge invariance, Phys. Lett. B **100**, 149 (1981).

[55] P. Orland and D. Rohrlich, Lattice gauge magnets: Local isospin from spin, Nucl. Phys. B **338**, 647 (1990).

[56] S. Chandrasekharan and U.-J. Wiese, Quantum link models: A discrete approach to gauge theories, Nucl. Phys. B **492**, 455 (1997).

[57] P. Hauke, D. Marcos, M. Dalmonte, and P. Zoller, Quantum Simulation of a Lattice Schwinger Model in a Chain of Trapped Ions, Phys. Rev. X **3**, 041018 (2013).

[58] J. Preskill, Quantum computing in the NISQ era and beyond, Quantum **2**, 79 (2018).

[59] J. Schwinger, Gauge invariance and mass. II, Phys. Rev. **128**, 2425 (1962).

[60] S. Coleman, R. Jackiw, and L. Susskind, Charge shielding and quark confinement in the massive Schwinger model, Ann. Phys. **275**, 267 (1975).

[61] E. Ercolessi, P. Facchi, G. Magnifico, S. Pascazio, and F. V. Pepe, Phase transitions in Z_n gauge models: Towards quantum simulations of the Schwinger-Weyl QED, Phys. Rev. D **98**, 074503 (2018).

[62] N. Bergeal, R. Vijay, V. E. Manucharyan, I. Siddiqi, R. J. Schoelkopf, S. M. Girvin, and M. H. Devoret, Analog information processing at the quantum limit with a Josephson ring modulator, Nat. Phys. **6**, 296 (2010).

[63] M. Kounalakis, C. Dickel, A. Bruno, N. K. Langford, and G. A. Steele, Tuneable hopping and nonlinear cross-Kerr interactions in a high-coherence superconducting circuit, npj Quantum Inf. **4**, 38 (2018).

[64] T. Roy, S. Kundu, M. Chand, S. Hazra, N. Nehra, R. Cosmic, A. Ranadive, M. P. Patankar, K. Damle, and R. Vijay, Implementation of Pairwise Longitudinal Coupling in a Three-Qubit Superconducting Circuit, Phys. Rev. Appl. **7**, 054025 (2017).

[65] T. Roy, S. Hazra, S. Kundu, M. Chand, M. P. Patankar, and R. Vijay, Programmable Superconducting Processor with Native Three-Qubit Gates, Phys. Rev. Appl. **14**, 014072 (2020).

[66] U. Vool and M. H. Devoret, Introduction to quantum electromagnetic circuits, Int. J. Circuit Theory Appl. **45**, 897 (2017).

[67] See Supplemental Material at http://link.aps.org/supplemental/10.1103/PhysRevB.103.235103 for more details about analytical derivations regarding the small version QLM, the circuit, and exact truncation, as well as a few details on our numerics, and more data of the Loschmidt echo rate function.

[68] P. Jordan and E. Wigner, Über das Paulische Äquivalenzverbot, Z. Phys. **47**, 631 (1928).

[69] L. Susskind, Lattice fermions, Phys. Rev. D **16**, 3031 (1977).

[70] D. Marcos, P. Rabl, E. Rico, and P. Zoller, Superconducting Circuits for Quantum Simulation of Dynamical Gauge Fields, Phys. Rev. Lett. **111**, 110504 (2013).

[71] C. G. Callan, R. F. Dashen, and D. J. Gross, The structure of the gauge theory vacuum, Phys. Lett. B **63**, 334 (1976).

[72] R. Jackiw and C. Rebbi, Vacuum Periodicity in a Yang-Mills Quantum Theory, Phys. Rev. Lett. **37**, 172 (1976).

[73] S. Coleman, More about the massive Schwinger model, Ann. Phys. **101**, 239 (1976).

[74] T. Schäfer and E. V. Shuryak, Instantons in QCD, Rev. Mod. Phys. **70**, 323 (1998).

[75] G. Gabadadze and M. Shifman, QCD vacuum and axions: What's happening?, Int. J. Mod. Phys. A **17**, 3689 (2002).

[76] R. D. Peccei, The strong CP problem and axions, Lect. Notes Phys. **741**, 3 (2008).

[77] R. D. Peccei, D. B. Tanner, and K. A. van Bibber, Why PQ?, in *AXIONS 2010: Proceedings of the International Conference*, edited by D. B. Tanner and K. A. van Bibber, AIP Conf. Proc. No. 1274 (AIP, New York, 2010), pp. 7–13.

[78] J. E. Kim and G. Carosi, Axions and the strong CP problem, Rev. Mod. Phys. **82**, 557 (2010).

[79] T. Fukui, Y. Hatsugai, and H. Suzuki, Chern numbers in discretized Brillouin zone: Efficient method of computing (spin) Hall conductances, J. Phys. Soc. Jpn. **74**, 1674 (2005).

[80] V. Berezinskiĭ, Destruction of long-range order in one-dimensional and two-dimensional systems possessing a continuous symmetry group. II. Quantum systems, Sov. J. Exp. Theor. Phys. **34**, 610 (1972).

[81] J. M. Kosterlitz and D. J. Thouless, Ordering, metastability, and phase transitions in two-dimensional systems, J. Phys. C **6**, 1181 (1973).

[82] A. Mitra, Time Evolution and Dynamical Phase Transitions at a Critical Time in a System of One-Dimensional Bosons after a Quantum Quench, Phys. Rev. Lett. **109**, 260601 (2012).

[83] L. Mathey, K. J. Günter, J. Dalibard, and A. Polkovnikov, Dynamic Kosterlitz-Thouless transition in two-dimensional Bose mixtures of ultracold atoms, Phys. Rev. A **95**, 053630 (2017).

[84] M. Fisher, The Nature of Critical Points, in *The Nature of Critical Points (Lectures in Theoretical Physics vol 7C)*, edited by W. E. Brittin and L. G. Dunham (University of Colorado Press, Boulder, 1965).

[85] T. W. B. Kibble, Topology of cosmic domains and strings, J. Phys. A: Math. Gen. **9**, 1387 (1976).

[86] W. H. Zurek, Cosmological experiments in superfluid helium?, Nature (London) **317**, 505 (1985).

[87] K. Shimizu, Y. Kuno, T. Hirano, and I. Ichinose, Dynamics of a quantum phase transition in the Bose-Hubbard model: Kibble-Zurek mechanism and beyond, Phys. Rev. A **97**, 033626 (2018).

[88] K. Roychowdhury, R. Moessner, and A. Das, Dynamics and correlations at a quantum phase transition beyond Kibble-Zurek, arXiv:2004.04162.

[89] D. Marcos, P. Widmer, E. Rico, M. Hafezi, P. Rabl, U.-J. Wiese, and P. Zoller, Two-dimensional lattice gauge theories with superconducting quantum circuits, Ann. Phys. **351**, 634 (2014).

[90] A. Mezzacapo, E. Rico, C. Sabín, I. L. Egusquiza, L. Lamata, and E. Solano, Non-Abelian SU(2) Lattice Gauge Theories in Superconducting Circuits, Phys. Rev. Lett. **115**, 240502 (2015).

[91] K. Le Hur, L. Henriet, A. Petrescu, K. Plekhanov, G. Roux, and M. Schiró, Many-body quantum electrodynamics networks: Non-equilibrium condensed matter physics with light, C. R. Phys. **17**, 808 (2016).

[92] M. J. Hartmann, Quantum simulation with interacting photons, J. Opt. **18**, 104005 (2016).

[93] G. K. Brennen, G. Pupillo, E. Rico, T. M. Stace, and D. Vodola, Loops and Strings in a Superconducting Lattice Gauge Simulator, Phys. Rev. Lett. **117**, 240504 (2016).

[94] H. Alaeian, C. W. S. Chang, M. V. Moghaddam, C. M. Wilson, E. Solano, and E. Rico, Creating lattice gauge potentials in circuit QED: The bosonic Creutz ladder, Phys. Rev. A **99**, 053834 (2019).

[95] N. Klco, E. F. Dumitrescu, A. J. McCaskey, T. D. Morris, R. C. Pooser, M. Sanz, E. Solano, P. Lougovski, and M. J. Savage, Quantum-classical computation of Schwinger model dynamics using quantum computers, Phys. Rev. A **98**, 032331 (2018).

[96] P. Roushan, C. Neill, A. Megrant, Y. Chen, R. Babbush, R. Barends, B. Campbell, Z. Chen, B. Chiaro, A. Dunsworth, A. Fowler, E. Jeffrey, J. Kelly, E. Lucero, J. Mutus, P. J. O'Malley, M. Neeley, C. Quintana, D. Sank, A. Vainsencher *et al.*, Chiral ground-state currents of interacting photons in a synthetic magnetic field, Nat. Phys. **13**, 146 (2017).

[97] Z.-H. Yang, Y.-P. Wang, Z.-Y. Xue, W.-L. Yang, Y. Hu, J.-H. Gao, and Y. Wu, Circuit quantum electrodynamics simulator of flat band physics in a Lieb lattice, Phys. Rev. A **93**, 062319 (2016).

[98] M. A. Nielsen, A simple formula for the average gate fidelity of a quantum dynamical operation, Phys. Lett. A **303**, 249 (2002).

[99] A. Gyenis, P. S. Mundada, A. Di Paolo, T. M. Hazard, X. You, D. I. Schuster, J. Koch, A. Blais, and A. A. Houck, Experimental realization of an intrinsically error-protected superconducting qubit, PRX Quantum **2**, 010339 (2021).

[100] M. Abuwasib, P. Krantz, and P. Delsing, Fabrication of large dimension aluminum air-bridges for superconducting quantum circuits, J. Vacuum Sci. Technol. B **31**, 031601 (2013).

[101] Z. Chen, A. Megrant, J. Kelly, R. Barends, J. Bochmann, Y. Chen, B. Chiaro, A. Dunsworth, E. Jeffrey, J. Y. Mutus, P. J. J. O'Malley, C. Neill, P. Roushan, D. Sank, A. Vainsencher, J. Wenner, T. C. White, A. N. Cleland, and J. M. Martinis, Fabrication and characterization of aluminum airbridges for superconducting microwave circuits, Appl. Phys. Lett. **104**, 052602 (2014).

[102] Z.-C. Jin, H.-T. Wu, H.-F. Yu, and Y. Yu, Fabrication of Al air-bridge on coplanar waveguide, Chin. Phys. B **27**, 100310 (2018).

[103] A. Dunsworth, R. Barends, Y. Chen, Z. Chen, B. Chiaro, A. Fowler, B. Foxen, E. Jeffrey, J. Kelly, P. V. Klimov, E. Lucero, J. Y. Mutus, M. Neeley, C. Neill, C. Quintana, P. Roushan, D. Sank, A. Vainsencher, J. Wenner, T. C. White *et al.*, A method for building low loss multi-layer wiring for superconducting microwave devices, Appl. Phys. Lett. **112**, 063502 (2018).

[104] H. Mukai, K. Sakata, S. J. Devitt, R. Wang, Y. Zhou, Y. Nakajima, and J.-S. Tsai, Pseudo-2D superconducting quantum computing circuit for the surface code: Proposal and preliminary tests, New J. Phys. **22**, 043013 (2020).

[105] V. Schmitt, Design, fabrication, and test of a four superconducting quantum-bit processor, Ph.D. theses, Université Pierre et Marie Curie, Paris, France, 2015.

[106] S. P. Pedersen, K. S. Christensen, and N. T. Zinner, Native three-body interaction in superconducting circuits, Phys. Rev. Research **1**, 033123 (2019).

[107] J. Koch, T. M. Yu, J. Gambetta, A. A. Houck, D. I. Schuster, J. Majer, A. Blais, M. H. Devoret, S. M. Girvin, and R. J. Schoelkopf, Charge-insensitive qubit design derived from the Cooper pair box, Phys. Rev. A **76**, 042319 (2007).

[108] P. Krantz, M. Kjaergaard, F. Yan, T. P. Orlando, S. Gustavsson, and W. D. Oliver, A quantum engineer's guide to superconducting qubits, Appl. Phys. Rev. **6**, 021318 (2019).

[109] M. A. Rol, F. Battistel, F. K. Malinowski, C. C. Bultink, B. M. Tarasinski, R. Vollmer, N. Haider, N. Muthusubramanian, A. Bruno, B. M. Terhal, and L. DiCarlo, Fast, High-Fidelity Conditional-Phase Gate Exploiting Leakage Interference in Weakly Anharmonic Superconducting Qubits, Phys. Rev. Lett. **123**, 120502 (2019).

[110] P. Zhao, P. Xu, D. Lan, J. Chu, X. Tan, H. Yu, and Y. Yu, High-contrast ZZ Interaction Using Superconducting Qubits with Opposite-Sign Anharmonicity, Phys. Rev. Lett. **125**, 200503 (2020).

[111] N. J. S. Loft, M. Kjaergaard, L. B. Kristensen, C. K. Andersen, T. W. Larsen, S. Gustavsson, W. D. Oliver, and N. T. Zinner, Quantum interference device for controlled two-qubit operations, npj Quantum Inf. **6**, 47 (2020).

[112] T. Bækkegaard, L. B. Kristensen, N. J. S. Loft, C. K. Andersen, D. Petrosyan, and N. T. Zinner, Realization of efficient quantum gates with a superconducting qubit-qutrit circuit, Sci. Rep. **9**, 13389 (2019).

[113] S. E. Rasmussen, K. S. Christensen, and N. T. Zinner, Controllable two-qubit swapping gate using superconducting circuits, Phys. Rev. B **99**, 134508 (2019).

[114] R. E. Barfknecht, S. E. Rasmussen, A. Foerster, and N. T. Zinner, Realizing time crystals in discrete quantum few-body systems, Phys. Rev. B **99**, 144304 (2019).

[115] K. Kasamatsu, I. Ichinose, and T. Matsui, Atomic Quantum Simulation of the Lattice Gauge-Higgs Model: Higgs Couplings and Emergence Of Exact Local Gauge Symmetry, Phys. Rev. Lett. **111**, 115303 (2013).

[116] H. Lamm, S. Lawrence, and Y. Yamauchi, Suppressing coherent gauge drift in quantum simulations, arXiv:2005.12688.

[117] J. C. Halimeh, V. Kasper, and P. Hauke, Fate of lattice gauge theories under decoherence, arXiv:2009.07848 [cond-mat.quant-gas].

[118] J. C. Halimeh and P. Hauke, Staircase prethermalization and constrained dynamics in lattice gauge theories, arXiv:2004.07248 [cond-mat.quant-gas].

[119] J. C. Halimeh and P. Hauke, Reliability of Lattice Gauge Theories, Phys. Rev. Lett. **125**, 030503 (2020).

[120] J. C. Halimeh, H. Lang, J. Mildenberger, Z. Jiang, and P. Hauke, Gauge-symmetry protection using single-body terms, arXiv:2007.00668 [quant-ph].

[121] J. C. Halimeh, R. Ott, I. P. McCulloch, B. Yang, and P. Hauke, Robustness of gauge-invariant dynamics against defects in ultracold-atom gauge theories, Phys. Rev. Research **2**, 033361 (2020).

[122] Z. Wang, S. Shankar, Z. K. Minev, P. Campagne-Ibarcq, A. Narla, and M. H. Devoret, Cavity attenuators for superconducting qubits, Phys. Rev. Appl. **11**, 14031 (2019).

[123] S. Touzard, A. Kou, N. E. Frattini, V. V. Sivak, S. Puri, A. Grimm, L. Frunzio, S. Shankar, and M. H. Devoret, Gated Conditional Displacement Readout of Superconducting Qubits, Phys. Rev. Lett. **122**, 080502 (2019).

[124] L. Qin, L. Xu, W. Feng, and X.-Q. Li, Qubit state tomography in a superconducting circuit via weak measurements, New J. Phys. **19**, 033036 (2017).

[125] M. Baur, A. Fedorov, L. Steffen, S. Filipp, M. P. da Silva, and A. Wallraff, Benchmarking a Quantum Teleportation Protocol in Superconducting Circuits Using Tomography and an Entanglement Witness, Phys. Rev. Lett. **108**, 040502 (2012).

[126] S. Filipp, P. Maurer, P. J. Leek, M. Baur, R. Bianchetti, J. M. Fink, M. Göppl, L. Steffen, J. M. Gambetta, A. Blais, and A. Wallraff, Two-Qubit State Tomography Using a Joint Dispersive Readout, Phys. Rev. Lett. **102**, 200402 (2009).

[127] L. Dicarlo, J. M. Chow, J. M. Gambetta, L. S. Bishop, B. R. Johnson, D. I. Schuster, J. Majer, A. Blais, L. Frunzio, S. M. Girvin, and R. J. Schoelkopf, Demonstration of two-qubit algorithms with a superconducting quantum processor, Nature (London) **460**, 240 (2009).

[128] M. Steffen, M. Ansmann, R. C. Bialczak, N. Katz, E. Lucero, R. McDermott, M. Neeley, E. M. Weig, A. N. Cleland, and J. M. Martinis, Measurement of the entanglement of two superconducting qubits via state tomography, Science **313**, 1423 (2006).

[129] J. Heinsoo, C. K. Andersen, A. Remm, S. Krinner, T. Walter, Y. Salathé, S. Gasparinetti, J.-C. Besse, A. Potočnik, A. Wallraff, and C. Eichler, Rapid High-Fidelity Multiplexed Readout of Superconducting Qubits, Phys. Rev. Appl. **10**, 34040 (2018).

[130] A. J. Daley, H. Pichler, J. Schachenmayer, and P. Zoller, Measuring Entanglement Growth in Quench Dynamics of Bosons in an Optical Lattice, Phys. Rev. Lett. **109**, 020505 (2012).

[131] H. Pichler, L. Bonnes, A. J. Daley, A. M. Läuchli, and P. Zoller, Thermal versus entanglement entropy: A measurement protocol for fermionic atoms with a quantum gas microscope, New J. Phys. **15**, 063003 (2013).

[132] R. Islam, R. Ma, P. M. Preiss, M. E. Tai, A. Lukin, M. Rispoli, and M. Greiner, Measuring entanglement entropy through the interference of quantum many-body twins, arXiv:1509.01160.

[133] N. M. Linke, S. Johri, C. Figgatt, K. A. Landsman, A. Y. Matsuura, and C. Monroe, Measuring the Rényi entropy of a two-site Fermi-Hubbard model on a trapped ion quantum computer, Phys. Rev. A **98**, 052334 (2018).

[134] T. Brydges, A. Elben, P. Jurcevic, B. Vermersch, C. Maier, B. P. Lanyon, P. Zoller, R. Blatt, and C. F. Roos, Probing Rényi entanglement entropy via randomized measurements, Science **364**, 260 (2019).